

NUCLEATION IN THE  
TWO-DIMENSIONAL ISING MODEL



# NUCLEATION IN THE TWO-DIMENSIONAL ISING MODEL

NUCLEATIE IN HET TWEE-DIMENSIONALE ISINGMODEL

(met een samenvatting in het Nederlands)

**Proefschrift**

TER VERKRIJGING VAN DE GRAAD VAN DOCTOR AAN DE  
UNIVERSITEIT UTRECHT OP GEZAG VAN DE RECTOR  
MAGNIFICUS, PROF. DR. W.H. GISPEN, INGEVOLGE  
HET BESLUIT VAN HET COLLEGE VAN PROMOTIES IN HET  
OPENBAAR TE VERDEDIGEN OP MAANDAG 9 JANUARI  
2006 DES OCHTENDS TE 10.30 UUR

DOOR

**Kevin Brendel**

GEBOREN OP 25 FEBRUARI 1977, TE AMSTERDAM

Promotor: Prof. dr. H. van Beijeren  
Copromotor: Dr. G.T. Barkema  
Faculteit Betawetenschappen, Universiteit Utrecht

# Contents

<b>1</b>	<b>Introduction</b>	<b>3</b>
1.1	Nucleation . . . . .	3
1.2	The Ising model . . . . .	5
1.3	Organization . . . . .	6
<b>2</b>	<b>Magnetization reversal times</b>	<b>9</b>
2.1	Introduction . . . . .	9
2.2	Theoretical framework . . . . .	10
2.3	Simulations and results . . . . .	13
2.3.1	Free energy landscape . . . . .	13
2.3.2	Interface diffusion coefficient . . . . .	16
2.3.3	Simulation results for magnetization reversal times . . . . .	17
2.3.4	Most slowly decaying mode . . . . .	24
2.4	Discussion . . . . .	24
<b>3</b>	<b>Nucleation times</b>	<b>31</b>
3.1	Introduction . . . . .	31
3.2	Theoretical framework . . . . .	33
3.3	Simulations and results . . . . .	37
3.3.1	Cluster free energies . . . . .	38
3.3.2	Interface diffusion coefficient . . . . .	39
3.3.3	Nucleation rates . . . . .	42
3.3.4	Short-time behavior . . . . .	45
3.4	Discussion . . . . .	49
<b>4</b>	<b>Mass fluctuations of a nucleating droplet</b>	<b>55</b>
4.1	Introduction . . . . .	55
4.1.1	Classical nucleation theory . . . . .	55
4.1.2	Detailed description of the model . . . . .	56

4.2	Fokker-Planck approach . . . . .	58
4.3	Simulation results for the cluster free energies . . . . .	60
4.4	Simulation results for the rate of growth and shrinkage . . . . .	64
4.5	Summary and conclusions . . . . .	64
<b>5</b>	<b>Fluctuations of the geomagnetic dipole</b>	<b>73</b>
5.1	Introduction . . . . .	73
5.2	Method . . . . .	74
5.3	Results on the HD model . . . . .	78
5.4	Results on Sint-800 data . . . . .	79
5.5	Conclusions and discussion . . . . .	80
	<b>Bibliography</b>	<b>81</b>
	<b>Samenvatting</b>	<b>87</b>
	<b>Curriculum Vitae</b>	<b>89</b>
	<b>Publications</b>	<b>89</b>

# Chapter 1

## Introduction

### 1.1 Nucleation

If a liquid, for instance water, is slowly cooled, there is a specific temperature below which it will crystallize; in the case of water, it becomes ice, and at atmospheric conditions, this happens at 273 K. During the solidification, the atoms organize themselves into a regular crystalline structure. The change from the liquid state to the crystalline solid state is a *phase transition*.

Also, if a gas is slowly cooled, there is a specific temperature below which it will condense into a liquid.

In both these cases, the phase transition is abrupt: water is liquid under atmospheric conditions at +0.01 degree Celsius, and solid ice at -0.01 degrees Celsius. And water is liquid at 99.99 degrees Celsius, but gaseous at 100.01 degrees Celsius. Such abrupt phase transitions are *first order* phase transitions.

If the condensation process is not initiated by impurities or by one of the boundaries, it usually occurs via the spontaneous birth of a tiny droplet, somewhere in the container, which then slowly grows, until eventually it incorporates the entire system. Such a slowly growing droplet is generally spherical in shape. The reason for the spherical shape is that there is a certain amount of free energy associated with each unit area of the interface between the liquid and gas. This additional free energy per unit area is known as the *surface tension*  $\sigma$ . The shape with the lowest area per unit of volume is a sphere, hence the spherical shape.

Associated with first order phase transitions is the possibility of supercooling or superheating: if pure water is cooled gently below 0 degrees

Celsius it will not freeze immediately, and likewise if it is heated above 100 degrees Celsius it will not vaporize immediately. The reason is connected with the phenomenon that small crystals or bubbles have a tendency to shrink, since the free energy cost of the surface dominates the free energy gain due to bulk difference in chemical potential. We can see this quantitatively by looking at the free energy as a function of the cluster radius  $R$ , for an isotropic macroscopic cluster:

$$F(R) = 4\pi R^2 \sigma - \frac{4\pi R^3}{3} \rho \Delta\mu, \quad (1.1)$$

where  $\rho$  is the number density of molecules in the cluster, and  $\Delta\mu$  the difference in chemical potential per molecule between the liquid and the solid state. If a cluster grows to a specific size, called the critical cluster size, the free energy reaches a maximum as a function of  $R$ , and the cluster will have equal probabilities to grow or to shrink. It may take a long time before there is a cluster that reaches this size.

Another word for such a cluster is the *nucleus* and the process described above is therefore called *homogeneous nucleation*; a strongly related, but different process is heterogeneous nucleation, in which one or more nuclei form near inhomogeneities such as impurities, or the wall of the container. The goal of this thesis is to improve the theoretical understanding of homogeneous nucleation, in particular to improve the estimates of nucleation times.

The starting point for our research is *classical nucleation theory* (CNT), which was founded in the first part of the last century by Volmer and Weber [14], Farkas [15], Becker and Döring [16] and Zeldovich [17], among others. In this theory, the nucleus grows and shrinks stochastically in steps of a single attaching or detaching molecule. At a given nucleus size, the ratio of the rates of growth and shrinkage is specified by using detailed balance; in the case of non-conserved processes as studied in this thesis, the common prefactor for both of these rates is assumed to be proportional to the interface area. In its simpler form, CNT makes the additional assumption that the surface tension of the nucleus equals the equilibrium surface tension of a flat, macroscopic interface, in the absence of a chemical potential difference. Thus the free energy is of the form (1.1) even for microscopic clusters.

In this thesis, we go beyond this simple theory. Specifically, in chapter 3 we measure the free energy as a function of nucleus size, without assuming that the surface tension of the nucleus equals the equilibrium surface tension of a flat, macroscopic interface, but still assuming that the common

prefactor for the rates of growth and shrinkage is proportional to the interfacial area. In chapter 4, we go further, and study this latter assumption.

## 1.2 The Ising model

One of the simplest models in which nucleation can be studied is the Ising model. We consider the Ising model on a  $B \times L$  rectangular lattice with periodic (helical) boundary conditions, with the Hamiltonian

$$H = -J \sum_{\langle i,j \rangle} s_i s_j + h \sum_i s_i, \quad (1.2)$$

in which  $s_i = \pm 1$  is the spin at site  $i$ ,  $J$  is the coupling constant, and  $h$  is the external magnetic field. The first summation runs over all pairs of nearest-neighbor sites; the nearest neighbors of site  $i$  are  $j = i \pm 1$  modulo  $N$  and  $j = i \pm B$  modulo  $N$ , with  $N = BL$ . The magnetization is defined as  $M \equiv \sum_i s_i$ ; it can take values  $M = -N, -N + 2, \dots, N$ ; all through this manuscript, we restrict ourselves to systems in which both  $B$  and  $L$  are even. As a consequence,  $M$  takes only even values, and summations over a range of possible magnetizations only run over even numbers, with an increment of 2.

A well-known property of the model is that at sufficiently low temperatures, in the absence of an external magnetic field, the distribution of the magnetization  $M \equiv \sum_i s_i$  becomes bimodal: the spins in a configuration tend to align, which causes  $M$  to fluctuate around one of the two preferred values  $\pm M_0$ . For infinite systems this occurs at all temperatures below the critical temperature  $T_c = J/(0.44069k_B)$ , for finite systems this range starts at slightly lower temperature.

In this thesis nucleation in the Ising model is studied by using Monte Carlo simulations. In these simulations the system evolves in time according to single-spin-flip dynamics with Metropolis acceptance probabilities [10]. If  $C_i$  is the configuration after  $i$  Monte Carlo steps, a trial configuration  $C'_{i+1}$  is generated by flipping a single spin at a random site. This trial configuration is then either accepted ( $C_{i+1} = C'_{i+1}$ ) or rejected ( $C_{i+1} = C_i$ ); the acceptance probability is given by

$$P_a = \min [1, \exp(-\beta(E(C'_{i+1}) - E(C_i)))] , \quad (1.3)$$

in which  $\beta = 1/(k_B T)$  with Boltzmann constant  $k_B$  and temperature  $T$ . The time scale is set such that in one unit of time, on average each site is visited once. So in our system, in one unit of time we perform  $BL$  Monte Carlo steps.

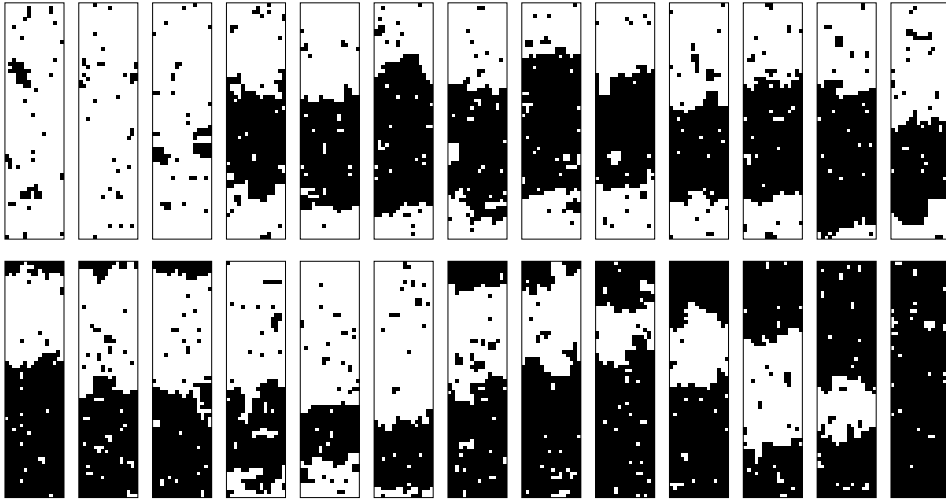


Figure 1.1: Snapshots of the transition at zero field from a state with most spins down to a state with most spins up in the  $16 \times 64$  Ising model, taken at equal time intervals of 500 attempted spin flips per site, at inverse temperature  $\beta J = 0.5$ .

### 1.3 Organization

The approach followed to study nucleation is to start with very simple models. In chapter 2 we study the Ising model without an external magnetic field. This system does not feature nucleation, but at low temperatures it jumps back and forth between a state in which most spins are up, to one in which most spins are down. The dominant pathway at low temperatures consists of the formation of a single pair of closed interfaces in the shorter periodic direction (for  $B \neq L$ ), which perform a relative diffusive motion around the longer periodic direction and annihilate after meeting each other through the periodic boundary. A series of snapshots, illustrating this process, is presented in figure 1.1. As will be shown in later chapters, understanding the dynamics of these interfaces is an important ingredient for our later studies of nucleation.

In chapter 3 we study the Ising model with an external field on a square lattice. Initially the system is in a metastable state, with most of the spins anti-aligned with the external field. It will stay in this metastable state for an extended period of time, but eventually one of the small clusters of aligned spins that arise due to fluctuations, will grow beyond the critical cluster size, and take over the whole system. After this, most of the spins

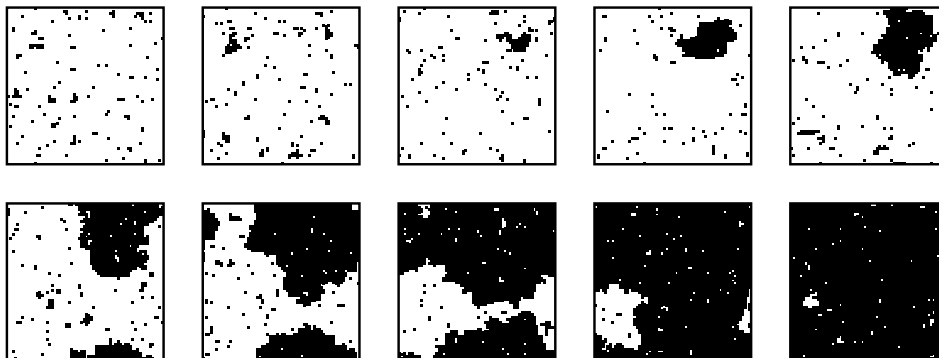


Figure 1.2: Snapshots of the the transition from a state with most spins down to a state with most spins up in the  $64 \times 64$  Ising model, taken at equal time intervals, at inverse temperature  $\beta J = 0.54$  and external field  $h = 0.08$ .

are aligned with the external field, and the system is in its stable state. A series of snapshots, illustrating this process, is presented in figure 1.2.

In chapter 4 the same model is studied. The effective rates of growth and shrinkage of clusters are now studied in detail. The mass of the nucleating cluster is followed in time, and mapped to a random walker undergoing drift and diffusion. The latter is described by the Fokker-Planck equation, in which in our case the drift and diffusion coefficients depend on cluster size.

The method developed in chapter 4 is then applied to a completely different phenomenon: the fluctuations of the geomagnetic dipole. Instead of to the time-evolution of the size of the nucleus, we apply our method of analysis, based on the Fokker-Planck equation, to the time-evolution of the strength of the geomagnetic dipole, which has been measured accurately over the last 800,000 years from fossile records [32]. This is described in chapter 5.

The chapters 2-5 correspond to four independent manuscripts [1, 2], in which only minor modifications were made (chapters 4 and 5 are yet to be published). Notably the explanation of the Ising model and its dynamics has been moved to the introduction. As a consequence some chapters contain parts that overlap significantly. A beneficial side effect is that, in combination with the introduction, each chapter can be read separately, as it is (almost) self-contained.



## Chapter 2

# Magnetization reversal times

### 2.1 Introduction

Activated processes that can be described with some type of Brownian dynamics are abundant in the world around us. Well-known examples are the nucleation of droplets in an undercooled gas or of crystals in an undercooled liquid, chemical reactions and the escape of a protein from a misfolded state. A prototype system to study such phenomena numerically is the well-known Ising model. Above the so-called critical temperature, in absence of an external magnetic field, up- and down-pointing spins are roughly equally abundant. Below the critical temperature, the system prefers to be in either of two states: one state with a positive magnetization in which most spins are pointing up, and one state with a negative magnetization. As long as the system size remains finite, reversals of the magnetization - transitions between positive and negative magnetization - are possible and will occur at a certain average frequency. These processes are activated, since configurations with magnetization close to zero have a much higher free energy than typical configurations with a magnetization close to either of the equilibrium values.

In this chapter, we study the time scales associated with magnetization reversal. A theoretical framework is outlined which is generally applicable to activated processes in systems with Brownian type dynamics, and compared to high-accuracy computer simulations. From a practical point of view magnetization reversals are also of great interest because of applications in memory devices and the like. One wants to have rapid switching of magnetization under reversals of an external field, but no spontaneous reversals of the magnetization, even if the external field has been turned off.

In the literature much attention has been paid to reversal time distributions in the presence of a driving field [3, 4]. In the fieldless case, much work has been done exactly at the critical temperature, see for instance [5]. Here, large-scale fluctuations in the magnetization decay at a time proportional to  $L^z$ , where  $z$  is the dynamical critical exponent. However, spontaneous reversals below the critical temperature in the absence of a field have hardly been studied. Here we consider the latter case for the prototypical case of an Ising model with periodic boundary conditions. We identify the leading scenario for reversals of the magnetization and show that the process may be described to a good approximation by a one-dimensional diffusion process over a potential barrier.

The lattice model which we study is the Ising model on a  $B \times L$  lattice with helical boundary conditions, as described in detail in chapter 1.

The chapter is organized as follows. In section 2.2, we outline our theoretical framework, which is generally applicable to activated processes in discrete systems with Brownian type dynamics. We then apply it to our specific study of magnetization reversal in the Ising model. In section 2.3 we compare the theoretical predictions with high-accuracy computational results.

## 2.2 Theoretical framework

To study the distribution of times between magnetization reversals at temperatures below the critical one we may consider an ensemble of a large number of systems prepared in states with a magnetization close to the equilibrium value  $-M_0$  and look at the rate at which these systems reach the value  $M = M_0$ , after which they are removed from the ensemble. Alternatively, the behavior of times between zero-crossings of the magnetization can be studied, as discussed below. The spin-flip dynamics described in the introductory chapter may be represented by a master equation for the probability distribution  $P(\sigma)$  of finding a system in the state  $\sigma$  at time  $t$ . Due to the huge number of possible states this master equation cannot be solved analytically or even numerically for system sizes of practical interest. Therefore, as an approximation we assume that we may replace the exact master equation by an approximate master equation for the probability  $P(M, t)$  of finding a system with magnetization  $M$  at time  $t$ . The form of

this equation is

$$\begin{aligned} \frac{dP(M, t)}{dt} &= \Gamma_{M, M+2}P(M+2, t) + \Gamma_{M, M-2}P(M-2, t) \\ &- (\Gamma_{M+2, M} + \Gamma_{M-2, M})P(M, t), \end{aligned} \quad (2.1)$$

with  $\Gamma_{M', M}$  the transition rate from  $M$  to  $M'$ . It ignores the fact that the actual transition rates will depend on the geometry of the state under consideration, with the idea that in typical cases spin states of very similar geometry will dominate the set of states with given  $M$ . Besides on  $M$  and  $\beta$  the transition rates will depend on the geometry of the system, that is on  $B$  and  $L$ . To estimate the scaling behavior of these dependencies we make two further simplifying assumptions:

- First of all, requiring  $B \leq L$ , we assume that states with  $M$  far from  $\pm M_0$  consist of a single strip of opposite magnetization separated by two phase boundaries of length  $B$  from the majority spin phase. The relevant changes of  $M$  then will be caused by displacements of these boundaries due to flips of spins along them. The total number of spins available for this will be proportional to  $B$ , hence the transition rates should also be proportional to  $B$  and independent of  $L$ .

This approximation will not be valid for values of  $M$  that are too close to  $\pm M_0$ , as for these the opposite magnetization will typically be found in a closed cluster rather than in a strip. It will turn out though that the contributions from these  $M$ -values to the reversal frequency are very small for systems of reasonable length. Therefore using the approximation  $\Gamma \sim B$  also here does not harm. Further we neglect the possibility of having more than one strip of opposite magnetization. When the temperature gets close to the critical one, when  $B$  becomes small or when  $L$  becomes very large, this may not be a good approximation. We will come back to this in section 2.4. In our further theoretical treatment we will assume that we are in a situation where the single-strip approximation is justified.

- Further we neglect changes due to fluctuations of the magnetization caused by the growth and shrinkage of small clusters of the minority spin type. On average these do not contribute to magnetization reversals, so this approximation should be allowed. In case one considers the first passage frequency through zero magnetization there is a small effect, to which we will come back in section 2.4 too.

In order that the equilibrium distribution be a stationary solution of the master equation we impose the condition of detailed balance

$$\frac{\Gamma_{M,M+2}}{\Gamma_{M+2,M}} = \exp[\beta(F(M) - F(M+2))], \quad (2.2)$$

where  $\beta F(M) = -\ln P_{eq}(M)$ , with  $P_{eq}(M)$  the equilibrium probability of magnetization  $M$ . In section 2.3.2 it will be explained how this condition may be combined with simulation results for interface diffusion to obtain approximations for all transition rates that lead to a good overall prediction of the reversal times.

The long-time reversal frequency as predicted by the master equation (2.1) follows as the largest eigenvalue of this equation, supplemented with an absorbing boundary at  $M = A$ , with either  $A = M_0$  or  $A = 0$ . The first choice corresponds to a real reversal of the magnetization, the second one to a first return to the value  $M = 0$ . After this the system will have equal probabilities to actually reverse its magnetization or to return to the equilibrium magnetization value it came from, hence this return frequency should be twice the reversal frequency. The absorbing boundary condition is implemented by setting  $\Gamma_{A-2,A}$  equal to zero.

The largest eigenvalue  $-\nu$  of  $\Gamma_{M,M'}$  in eq. (2.1), as well as the corresponding eigenvector  $P_0(M)$ , may be found by requiring that the net current away from magnetization  $M$  assumes the value  $\nu P_0(M)$ . Using conservation of probability one easily checks that this may be expressed as

$$\Gamma_{M+2,M}P_0(M) - \Gamma_{M,M+2}P_0(M+2) = \nu \sum_{m \leq M} P_0(m), \quad (2.3)$$

$$\nu = \frac{\Gamma_{A,A-2}P_0(A-2)}{\sum_{m \leq A-2} P_0(m)}. \quad (2.4)$$

In eq. (2.3)  $P_0(m)$  on the right hand side may be approximated, up to a normalization factor, by  $\exp(-\beta F(m))$ , because the sum is dominated by the terms with small  $m$ -values, for which this approximation is excellent. This one may check in hindsight against the solution obtained. With this approximation the equation may be solved recursively for  $P_0(M)$  in terms of  $P_0(A-2)$  for  $M = A-4, A-6, \dots$ , with the result

$$\begin{aligned} P_0(M) &= \sum_{M \leq m \leq A-2} \frac{\Gamma_{A,A-2}}{\Gamma_{m+2,m}} \exp[\beta(F(m) - F(M))] \\ &\times \frac{\sum_{n \leq m} \exp[-\beta F(n)]}{\sum_{n' \leq A-2} \exp[-\beta F(n')]} P_0(A-2). \end{aligned} \quad (2.5)$$

The summations over  $m$  and  $M$  are dominated by values of  $m$  close to zero, combined with values for  $M$  close to  $-M_0$ , for which the sum over  $n$  is basically independent of  $m$ . Therefore the reversal frequency may be obtained as

$$\begin{aligned} \nu &= \frac{\Gamma_{A,A-2} P_0(A-2)}{\sum_{M \leq A-2} P_0(M)} \\ &= \left( \sum_{m=-M_0}^{A-2} \frac{\exp[\beta F(m)]}{\Gamma_{m+2,m}} \sum_{n \leq A-2} \exp[-\beta F(n)] \right)^{-1}. \end{aligned} \quad (2.6)$$

The restriction of the summation over  $m$  to values  $m > -M_0$  is needed to avoid large spurious contributions from  $m < -M_0$ . The result in eq. (2.6) is well-known. It is usually derived by considering a state with a stationary current in which mass is inserted at a constant rate on one side (e.g. at  $M = -B \times L$  in our case) and taken out as soon as it reaches the absorbing boundary (see e.g. [6], section IV E). In that case the replacement of the sum over  $n$  by a constant is exact.

## 2.3 Simulations and results

In order to apply the above theoretical framework to magnetization reversal times in the Ising model, the two ingredients required are: (i) the equilibrium probability  $P_{eq}(M)$  to find the system in a state with magnetization  $M$ ; and (ii) the transition rates  $\Gamma_{M',M}$  from magnetization  $M$  to  $M'$ . We obtain these two ingredients via two different computational approaches.

### 2.3.1 Free energy landscape

For various values of  $L$  and  $B$  and various temperatures we make histograms of the joint distribution of the magnetization  $M = \sum_i \sigma_i$  and the energy. Since the probability that a state with energy  $E$  occurs at an inverse temperature  $\beta$  is proportional to the Boltzmann weight  $\exp(-\beta E)$ , a histogram made at a certain temperature provides information about the probability distribution at nearby temperatures as well. We use the multiple histogram method [7] to combine the information from simulations at various temperatures. In this way, histograms for the magnetization over a wide range of temperatures can be obtained from relatively few simulations. As defined above, the free energy  $F(M)$  is related to the probability that a certain magnetization  $M$  occurs by  $P_{eq}(M) = e^{-\beta F(M)}$ . The method

of determining free energies of configurations constrained to some value of a coordinate along a pathway through phase space has been used extensively, for instance by Auer and Frenkel [8]. In figure 2.1 the free energy as a function of the magnetization per spin  $m = M/N$  is plotted at two different temperatures and three different values of  $L/B$ .

In order to compare these results with theory we note that the probability  $P_{eq}(0)$  of finding the system in a state with  $M = 0$  can be obtained from eq. (4.23) of chapter V of [9] as follows. First note that this equation gives the following approximation for the partition function of a periodic anti-ferromagnetic system with one phase boundary [11], which is equivalent to a ferromagnetic system with an anti-periodic boundary:

$$Z_1 = \frac{Z_0}{2} \sum_{k=1}^{2L} \left( \frac{A(k) - \sqrt{A^2(k) - c^2}}{A(k) + \sqrt{A^2(k) - c^2}} \right)^{B/2}, \quad (2.7)$$

where

$$\begin{aligned} A(k) &= (1 + z^2)^2 - 2z(1 - z^2) \cos \frac{\pi k}{L}, \\ c &= 2z(1 - z^2), \\ z &= \tanh \beta J, \end{aligned}$$

and  $Z_0$  the partition function for a homogeneous system (cf. (4.20) of [9]). Neglecting the possible interaction between two phase boundaries (or interfaces) we conclude that the partition function  $Z_2$  for a system with two interfaces is given by  $Z_2/Z_0 = (1/2)(Z_1/Z_0)^2$ . The factor 1/2 arises because otherwise we would count each configuration twice: interchanging the locations of the two interfaces does not give a different configuration. If we leave the positions of the two interfaces completely free the magnetization is distributed almost uniformly over all possible even values between  $-M_0$  and  $M_0$ . Therefore, fixing  $M$  to 0 leads to a reduction of the partition function by a factor of  $M_0$ . Thus we arrive at the following result for  $P_{eq}(0)$ :

$$\begin{aligned} P_{eq}(0) &= \frac{Z_2}{M_0 Z_0} \\ &= \frac{1}{8M_0} \left[ \sum_{k=1}^{2L} \left( \frac{A(k) - \sqrt{A^2(k) - c^2}}{A(k) + \sqrt{A^2(k) - c^2}} \right)^{B/2} \right]^2. \end{aligned} \quad (2.8)$$

For square systems this result has to be modified, because there are two ways to make a strip with opposite magnetization: the interfaces can lie in

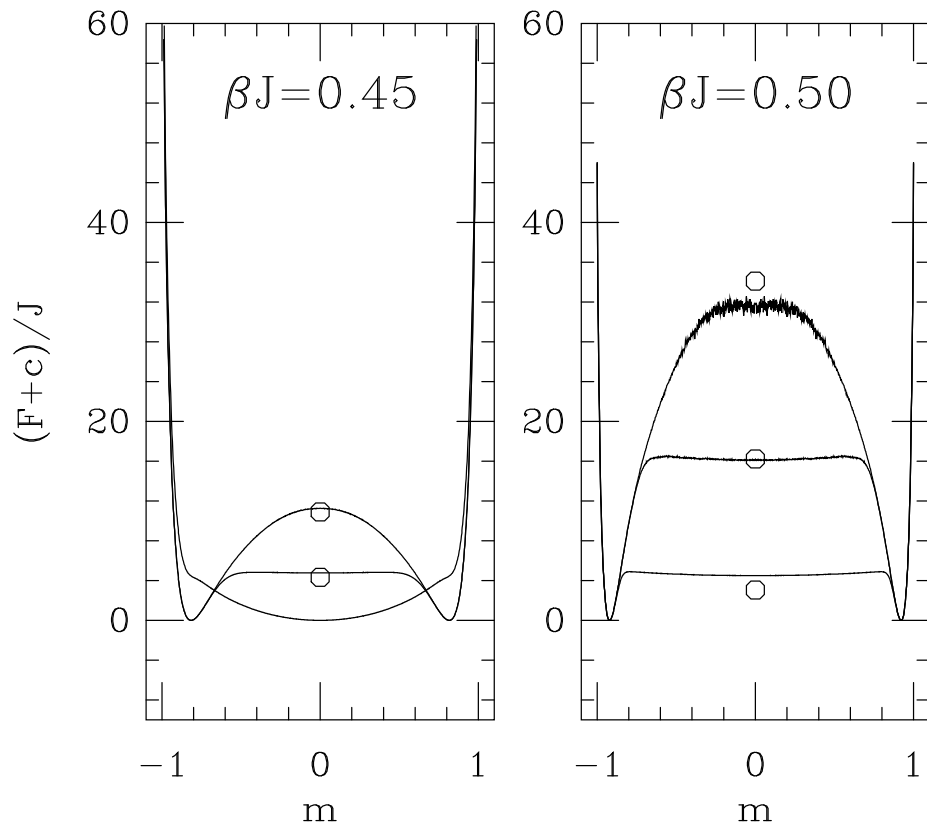


Figure 2.1: Free energy (in units of  $J$ ) as a function of magnetization at inverse temperatures  $\beta J = 0.45$  and  $\beta J = 0.50$ . The number of spins is kept constant at 1024. The solid lines represent the  $32 \times 32$  system, the dotted lines represent the  $16 \times 64$  system, and the dash-dotted lines represent the  $8 \times 128$  system. The free energies at  $M = 0$  corresponding to equation (2.8) are also indicated. A constant is added to the free energy curves, such that the minimal value of  $F(M)$  is zero in all cases.

the horizontal as well as in the vertical direction. This gives an additional factor 2 in the equation for  $P_{eq}(0)$ .

### 2.3.2 Interface diffusion coefficient

The second ingredient for the theoretical framework in section 2.2 consists of the transition rates  $\Gamma_{M',M}$  from magnetization  $M$  to  $M'$ . As discussed there, we are actually mostly interested in the contribution to the transition rates that arises from the diffusion parallel to the longer periodic direction of interfaces that span the shorter one. To estimate this diffusion coefficient numerically, we study systems with anti-periodic boundary conditions: the spins in two neighboring sites  $i < N - 1$  and  $j = i + 1$ , or in  $i < N - B$  and  $j = i + B$  are aligned if  $\sigma_i = \sigma_j$ , whereas the spins in two neighboring sites  $i = N - 1$  and  $j = 0$ , or in  $i \geq N - B$  and  $j = i + B - N$ , are aligned if  $\sigma_i = -\sigma_j$ .

The interface location  $x(0)$  is initially defined as the magnetization  $M(0)$ . As long as  $M \in [-0.8N, 0.8N]$ , steps  $\Delta x$  in the interface location are equal to changes  $\Delta M$  in the magnetization, *i.e.*,  $x(t + \Delta t) - x(t) = M(t + \Delta t) - M(t)$ . Once the interface gets close to the anti-periodic boundary, the magnetization does not uniquely determine the interface location. As soon as  $M$  is no longer in the interval  $[-0.8N, 0.8N]$ , we shift the anti-periodic boundary away from the interface over half the system size (which will bring the magnetization back in this range) and then continue.

In practice, we achieve this by switching from monitoring  $M$  to monitoring  $M' = \sum_{i=0}^{N/2-1} \sigma_i - \sum_{i=N/2}^{N-1} \sigma_i$ , and  $|x(t + \Delta t) - x(t)| = |M'(t + \Delta t) - M'(t)|$ . The sign of the steps in  $x(t)$  depends on the location of the interface: in the lower half this sign will be unchanged, whereas in the upper half it will be reversed. As soon as  $M'$  leaves the interval  $[-0.8N, 0.8N]$  we switch back to measuring steps in the original magnetization  $M$ . Also here, the sign of the steps in  $x(t)$  depends on the location of the interface. Note that  $x$  is not confined to the interval  $[-N, N]$ . The diffusion coefficient  $D$  is then obtained from the time-dependent interface location  $x(t)$  as

$$D = \lim_{t \rightarrow \infty} \left[ \frac{\langle (x(t) - x(0))^2 \rangle}{2t} \right]. \quad (2.9)$$

We expect that the interface diffusion is independent of  $L$ , and that it grows linearly with  $B$  since the number of sites where a spin flip moves the interface grows linearly with its width; however, for small  $B$  corrections

arise due to the periodicity (or helicity) of the boundaries. Consequently, we expect

$$D(B, L, \beta J) = g(\beta J)B + c. \quad (2.10)$$

For temperatures close to  $T_c$  and small  $B$ , the system might occasionally contain more than a single interface. In that case, equation (2.9) would overestimate the diffusion coefficient of an interface. Since the additional free energy cost of interfaces increases linearly with  $B$ , this unwanted contribution to  $D$  decreases exponentially with  $B$ . Taking this into account, our approach is to measure for various values of  $\beta J$ ,  $B$ , and  $L$  the diffusion coefficient  $D$  via eq. (2.9). Next we determine the function  $g(\beta J)$  in equation (2.10); the results are plotted in figure 2.2. Indeed we find that for increasing  $B$  and at temperatures not too close to  $T_c$  the diffusion coefficient rapidly becomes independent of  $L$  within the ranges of  $L$ -values we considered. In our theoretical framework we then use as approximation for the jump rates

$$\min[\Gamma_{M, M+2}, \Gamma_{M+2, M}] = \frac{g(\beta J)B}{2}. \quad (2.11)$$

This may be understood from the observations that on the one hand one has  $D = 4\Gamma$ , because the jumps in magnetization go by units of 2, on the other hand  $D$  satisfies (2.10) with  $B$  replaced by  $2B$  because there are two interfaces. The above equation, in combination with eq. (2.2) and the free energy as a function of magnetization, specifies all the transition rates. Using (2.6) we can now predict the magnetization reversal times. The results are shown in Table 2.1.

### 2.3.3 Simulation results for magnetization reversal times

We measure the magnetization every  $N$  attempted spin flips. We look for events where the magnetization crosses from positive (more than half the spins up) to negative or vice versa between two consecutive measurements.

We make histograms of the times between two occurrences of magnetization reversal events. The histogram obtained in a system containing  $16 \times 64$  spins, at the temperature corresponding to  $\beta J = 0.45$ , is shown in figure 2.3. For comparison we also show a histogram of the times measured between the first time the system reaches a free energy minimum, and the first time after this it reaches the other minimum. We will come back to this in our discussion.

The figure shows that at long times the decay function  $f(t)$  behaves as  $f(t) \sim \exp(-t/\tau)$ . Here, we focus on the long-time behavior, and are

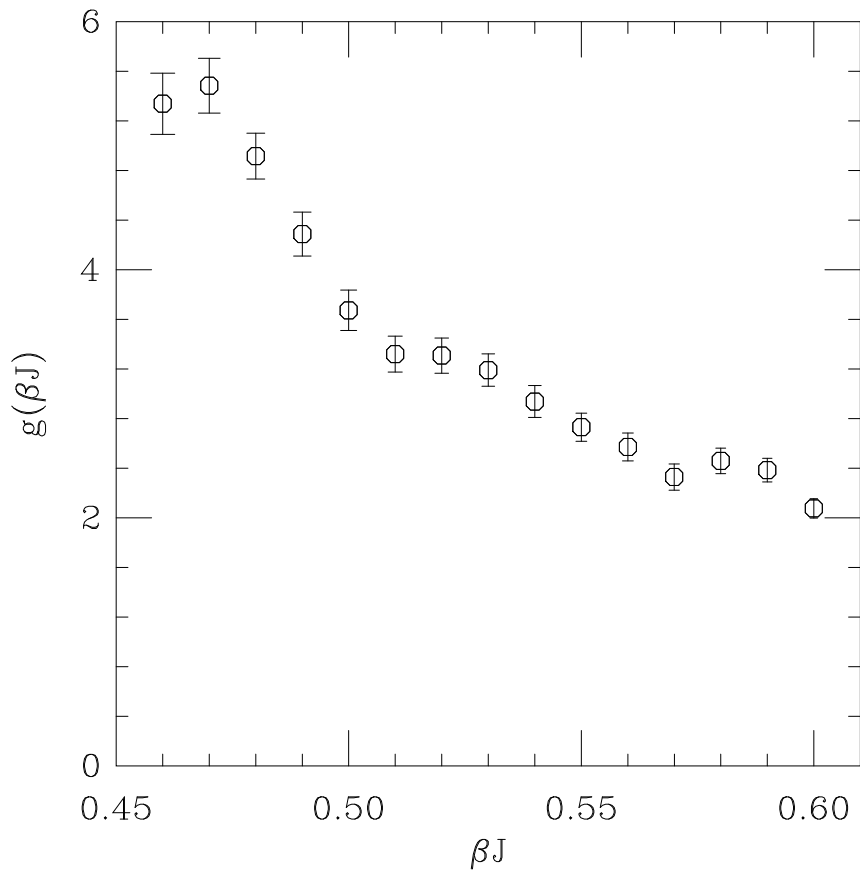


Figure 2.2: Monte Carlo measurements of the diffusion coefficient per interface length  $g(\beta J)$ , as a function of inverse temperature  $\beta J$ .

Table 2.1: Estimated values for the magnetization reversal times.

$\beta J$	$32 \times 32$	$16 \times 64$	$16 \times 32$
0.46	$1.66 \times 10^5$	$1.74 \times 10^4$	$1.19 \times 10^4$
0.47	$1.12 \times 10^6$	$4.21 \times 10^4$	$3.15 \times 10^4$
0.48	$8.88 \times 10^6$	$1.25 \times 10^5$	$9.96 \times 10^4$
0.49	$7.38 \times 10^7$	$3.97 \times 10^5$	$3.31 \times 10^5$
0.50	$6.49 \times 10^8$	$1.31 \times 10^6$	$1.12 \times 10^6$
0.51	$5.83 \times 10^9$	$4.19 \times 10^6$	$3.61 \times 10^6$
0.52	$5.31 \times 10^{10}$	$1.23 \times 10^7$	$1.05 \times 10^7$
0.53	$5.77 \times 10^{11}$	$3.78 \times 10^7$	$3.11 \times 10^7$
0.54	$7.69 \times 10^{12}$	$1.23 \times 10^8$	$9.60 \times 10^7$
	$16 \times 16$	$8 \times 64$	$8 \times 32$
0.46	$4.43 \times 10^3$	$2.76 \times 10^3$	$1.24 \times 10^3$
0.47	$1.06 \times 10^4$	$3.26 \times 10^3$	$1.73 \times 10^3$
0.48	$3.09 \times 10^4$	$4.72 \times 10^3$	$2.88 \times 10^3$
0.49	$9.56 \times 10^4$	$7.45 \times 10^3$	$5.11 \times 10^3$
0.50	$3.09 \times 10^5$	$1.26 \times 10^4$	$9.47 \times 10^3$
0.51	$9.60 \times 10^5$	$2.12 \times 10^4$	$1.69 \times 10^4$
0.52	$2.73 \times 10^6$	$3.32 \times 10^4$	$2.77 \times 10^4$
0.53	$8.06 \times 10^6$	$5.50 \times 10^4$	$4.71 \times 10^4$
0.54	$2.50 \times 10^7$	$9.69 \times 10^4$	$8.43 \times 10^4$
0.55	$7.64 \times 10^7$	$1.70 \times 10^5$	$1.49 \times 10^5$
0.56	$2.30 \times 10^8$	$2.96 \times 10^5$	$2.61 \times 10^5$
0.57	$7.20 \times 10^8$	$5.38 \times 10^5$	$4.75 \times 10^5$
0.58	$1.92 \times 10^9$	$8.37 \times 10^5$	$7.39 \times 10^5$
0.59	$5.54 \times 10^9$	$1.42 \times 10^6$	$1.25 \times 10^6$
0.60	$1.77 \times 10^{10}$	$2.66 \times 10^6$	$2.34 \times 10^6$

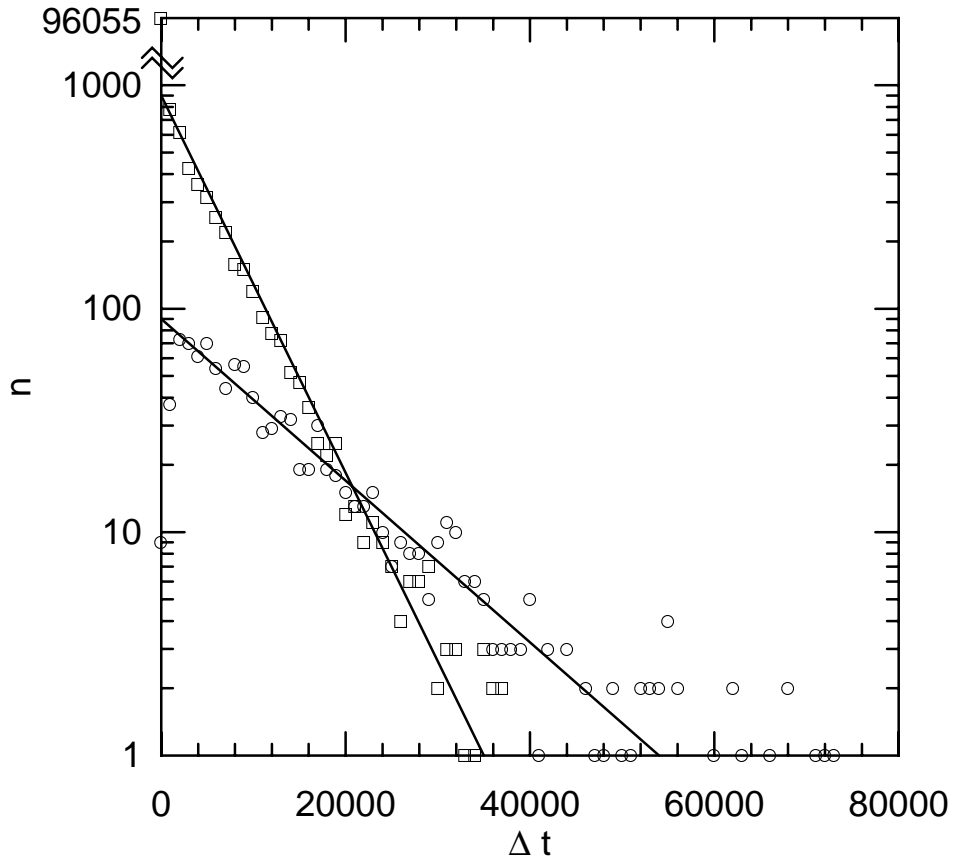


Figure 2.3: Histogram of the times between subsequent zero-crossings of the magnetization (squares), and the times between subsequent first occurrences of a free energy minimum with opposite magnetization in the  $16 \times 64$  Ising model at  $\beta J = 0.45$ . The solid lines depict the fits to the data, obtained as described in the main text.

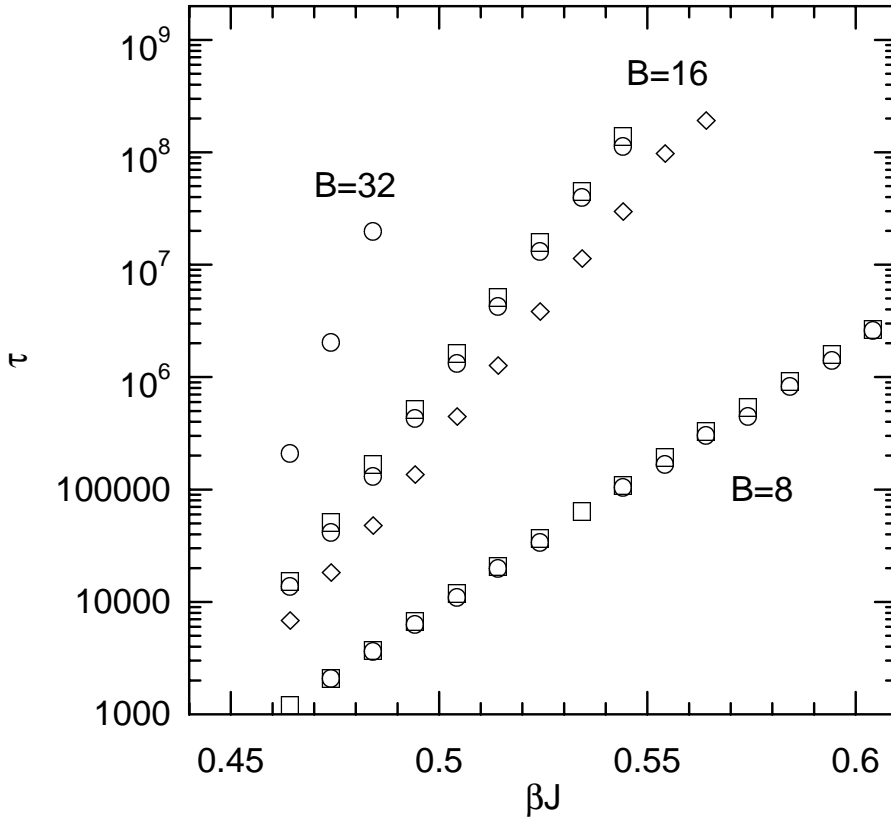


Figure 2.4: Magnetization reversal times  $\tau$  versus inverse temperature  $\beta J$ , for various system sizes. The diamonds, circles and squares represent systems with  $L = 16, 32$  and  $64$ , respectively.

specifically interested in the escape time  $\tau$ . We obtain this quantity via a fitting procedure, in which we ignore the data up to a time  $t_0$ , chosen such that  $f(t)$  shows exponential time behavior for  $t > t_0$ . Then we determine the time  $t'$  at which half of the remaining events have taken place. The escape time  $\tau$  is then obtained from  $\tau = (t' - t_0)/\ln(2)$ . Instead we could have made a linear fit of all the data points beyond  $t_0$ , but this makes no significant difference.

The resulting reversal times, for several system sizes and inverse temperatures, are presented in Table 2.2 and plotted in figure 2.4.

Table 2.2: Directly measured values for the magnetization reversal times.

$\beta J$	$32 \times 32$	$16 \times 64$	$16 \times 32$
0.46	$2.09(6) \times 10^5$	$1.52(3) \times 10^4$	$1.37(1) \times 10^4$
0.47	$2.02(6) \times 10^6$	$5.14(5) \times 10^4$	$4.18(4) \times 10^4$
0.48	$1.97(6) \times 10^7$	$1.68(1) \times 10^5$	$1.32(1) \times 10^5$
0.49		$5.20(5) \times 10^5$	$4.26(6) \times 10^5$
0.50		$1.62(5) \times 10^6$	$1.33(2) \times 10^6$
0.51		$5.2(1) \times 10^6$	$4.28(6) \times 10^6$
0.52		$1.59(5) \times 10^7$	$1.32(3) \times 10^7$
0.53		$4.5(2) \times 10^7$	$4.0(1) \times 10^7$
0.54		$1.40(6) \times 10^8$	$1.13(4) \times 10^8$
	$16 \times 16$	$8 \times 64$	$8 \times 32$
0.46	$6.83(7) \times 10^3$	$1.21(1) \times 10^3$	$1.23(1) \times 10^3$
0.47	$1.81(2) \times 10^4$	$2.10(2) \times 10^3$	$2.08(2) \times 10^3$
0.48	$4.8(2) \times 10^4$	$3.75(3) \times 10^3$	$3.61(4) \times 10^3$
0.49	$1.35(4) \times 10^5$	$6.70(7) \times 10^3$	$6.30(6) \times 10^3$
0.50	$4.45(4) \times 10^5$	$1.20(1) \times 10^4$	$1.11(1) \times 10^4$
0.51	$1.26(1) \times 10^6$	$2.07(2) \times 10^4$	$1.99(2) \times 10^4$
0.52	$3.82(5) \times 10^6$	$3.66(3) \times 10^4$	$3.37(3) \times 10^4$
0.53	$1.13(2) \times 10^7$	$6.36(6) \times 10^4$	$5.87(5) \times 10^4$
0.54	$2.97(6) \times 10^7$	$1.09(1) \times 10^5$	$1.04(2) \times 10^5$
0.55	$9.7(3) \times 10^7$	$1.95(3) \times 10^5$	$1.68(3) \times 10^5$
0.56	$1.9(2) \times 10^8$	$3.26(6) \times 10^5$	$3.05(9) \times 10^5$
0.57		$5.40(8) \times 10^5$	$4.5(1) \times 10^5$
0.58		$9.2(2) \times 10^5$	$8.3(2) \times 10^5$
0.59		$1.61(2) \times 10^6$	$1.41(3) \times 10^6$
0.60		$2.67(5) \times 10^6$	$2.64(8) \times 10^6$

One sees by comparing the results of Tables I and II that in most cases the two agree within 20% for temperatures not too close to the critical temperature.

A commonly used first approximation to the description of the time scales of activated processes is Arrhenius' law, which states that the typical time scale  $\tau$  increases exponentially with the height of the (free) energy barrier  $\Delta F \equiv F(M = 0) - F(M = M_0)$ , with a prefactor  $f$  that depends in a mild way on temperature and system size,

$$\tau = f(\beta, B, L) \exp(\beta\Delta F). \quad (2.12)$$

If we straightforwardly use the free energy  $F(M)$  as defined before we can obtain the heights of the free-energy barriers directly from the histograms of the magnetization distribution. To check the accuracy of this, we have plotted in figure 2.5 the ratio of  $\tau$  and  $\exp(\beta\Delta F)$  as a function of inverse temperature  $\beta J$ , for various system sizes. Clearly, if the prefactor  $f$  is assumed to be constant, this simple approximation fails to even predict the magnetization reversal times within an order of magnitude.

A little thought reveals that, in the present case, this way of determining the free energy barrier is not entirely satisfactory. The reason is that for magnetization values around  $M = M_0$  the free energy increases with system size because the range of values through which  $M$  typically fluctuates, increases as the square root of system size. As a consequence the probability of finding any specific  $M$ -value decreases. Around  $M = 0$  on the other hand, no similar effect occurs, due to the wide plateau of the free energy as function of  $M$ . As a result of this the decrease of probability of finding a given magnetization value for given relative position of the two interfaces is precisely compensated by the probabilities of finding this same magnetization value at different relative positions. Therefore it makes more sense in this case to define the Arrhenius factor in an alternative way as  $\exp(\beta F(M = 0))$ . With this definition, where again  $\beta F(M) = -\ln(P_{eq}(M))$ , it may be interpreted indeed as the equilibrium probability of finding two interfaces dividing the system into equal areas. But please notice that if, instead of a plateau, the free energy has a maximum of a width small compared to the range of magnetization fluctuations, the first definition of the Arrhenius factor is to be preferred.

With the second definition the expression for the decay time in terms of the Arrhenius factor becomes

$$\tau = f'(\beta, B, L) \exp(\beta F(M = 0)), \quad (2.13)$$

in which again one hopes that the prefactor  $f'$  depends on temperature and system dimensions only in a mild way. On the basis of (2.6) and (2.11) we may conclude that for large systems  $f'$  should simply be proportional to  $L$  and independent of  $B$ .

Figure 2.6 shows  $f'$  as a function of inverse temperature for several system sizes. For  $L = 32$  and  $64$  both the approximate independence of  $B$  and the proportionality to  $L$  are quite well-confirmed, especially if one takes into account that the plateau widths for these system sizes are notably less than  $L$  (see figure 2). For  $L = 16$  the plateau becomes so narrow that the above predictions do not apply.

### 2.3.4 Most slowly decaying mode

To obtain an estimate for the magnetization reversal times, we first estimated the most slowly decaying mode in eq. (2.5). Besides comparing the magnetization reversal times, we can also obtain the most slowly decaying eigenmode  $P_0(M)$  directly from our Monte Carlo simulations by measuring the probability difference between the occurrence of a certain magnetization  $M$  and the occurrence of the opposite magnetization  $-M$ , averaged over a time scale comparable to the magnetization reversal time  $\tau$ . Since  $P_0$  decays much slower than the other antisymmetric (in  $M$ ) modes, it will give the dominant contribution to this probability difference. Figure 2.7 compares the most slowly decaying eigenmode as obtained with eq. (2.5) with the direct Monte Carlo measurements, for the  $16 \times 64$  system at  $\beta J = 0.5$ .

## 2.4 Discussion

Our simulations confirm the global picture we sketched for the process of magnetization reversals in the Ising model with stochastic dynamics: a large cluster of opposite magnetization, originating through a fluctuation develops into a pair of interfaces. These interfaces diffuse around the system and annihilate, leaving the system in the oppositely magnetized phase. Quantitatively this process may be described to a good approximation as a diffusion process in a one-dimensional space with a coordinate describing the total magnetization in the system.

A few remarks should be made here.

- First of all it may seem remarkable that in almost all cases our theoretical prediction gives a shorter reversal time than the simulations. Since the theory neglects processes that enhance the reversal

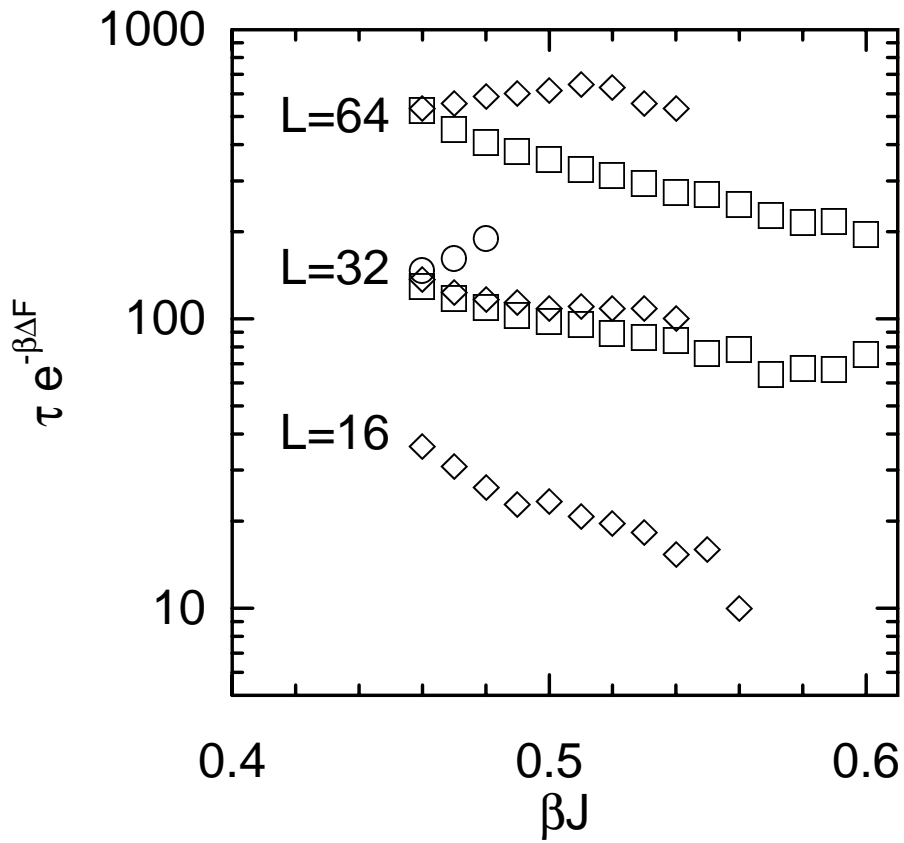


Figure 2.5: Magnetization reversal times  $\tau$  divided by the Arrhenius factor  $\exp(\beta\Delta F)$ , plotted against inverse temperature  $\beta J$ , for various system sizes. The squares, diamonds and circles represent systems with  $B = 8, 16$  and  $32$ , respectively.

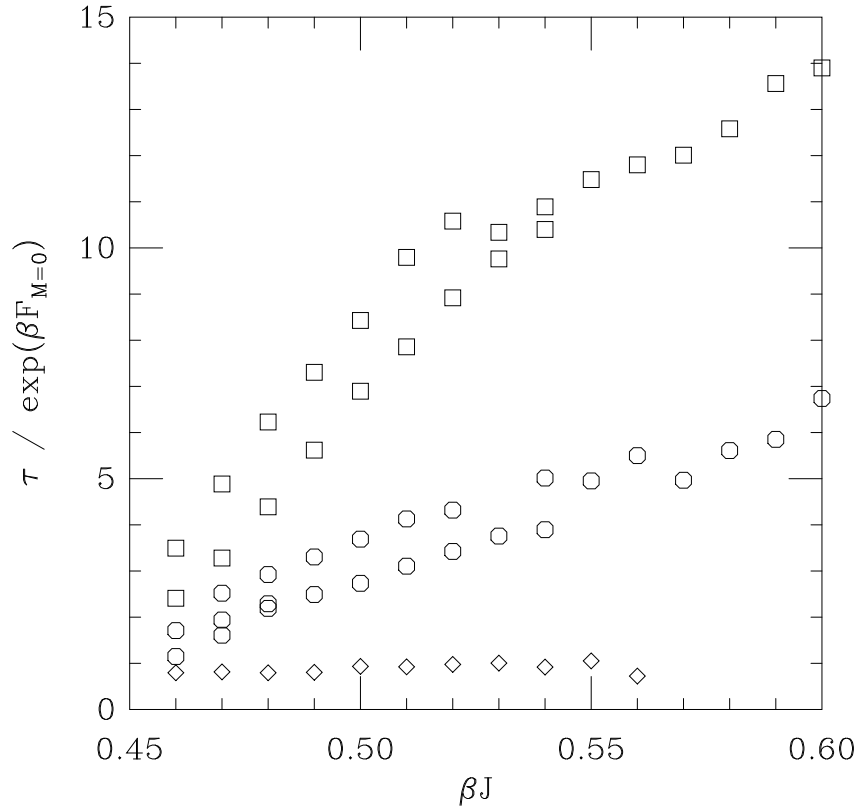


Figure 2.6: Magnetization reversal times  $\tau$  divided by  $\exp(\beta F(0)) \equiv P_{eq}(M=0)^{-1}$ , as function of inverse temperature  $\beta J$ , for various system sizes. The squares, circles and diamonds represent systems with  $L = 64$ , 32 and 16.

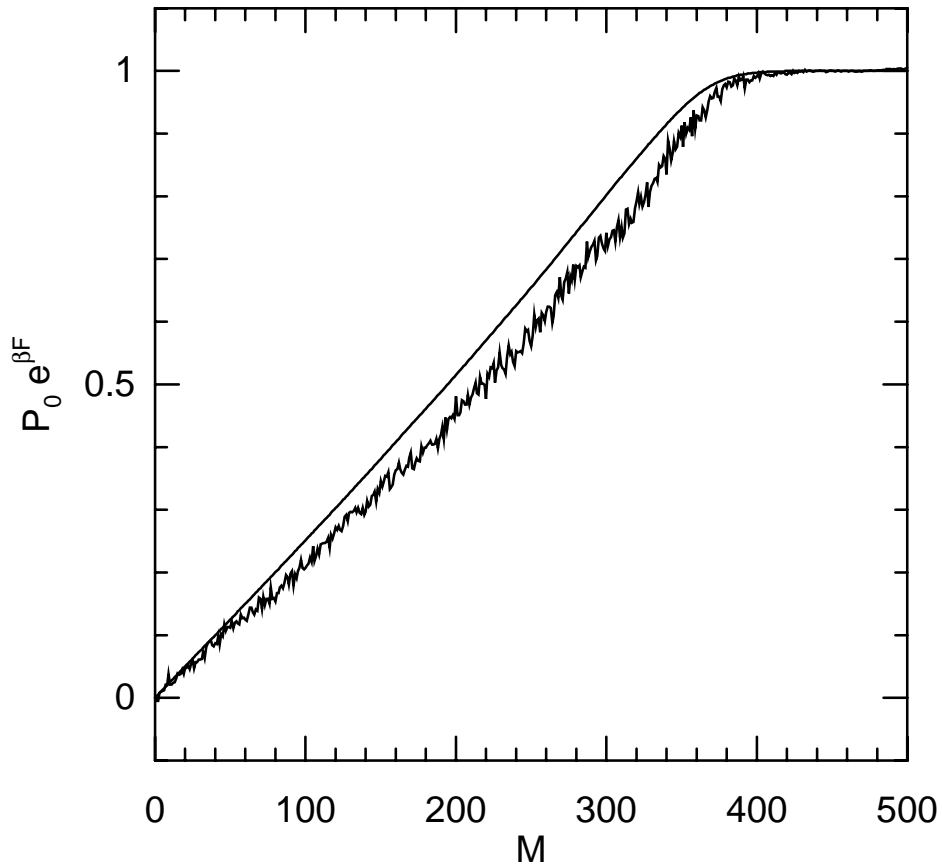


Figure 2.7: The most slowly decaying eigenmode  $P_0(M)$  divided by the stationary model, in other words by the equilibrium distribution  $\exp(-\beta F(M))$  for the  $16 \times 64$  system at  $\beta J = 0.5$ . The wavy and the smooth lines give, respectively, the simulation results and the theoretical prediction. Since this function is antisymmetric in  $M$ , the left hand side of the figure ( $M < 0$ ) has been left out for clarity.

frequency, such as the formation of more than two simultaneous interfaces and spurious passages of  $M = 0$  (see below), one might expect an overestimate of the reversal time rather than an underestimate. The explanation of the latter comes primarily from that part of the process in which a growing cluster of opposite magnetization transforms into a band around the cylinder. As the cluster will at first be typically circular in shape (if the temperature is not too low) it has to deform into more elliptical shape, with a longer interface than the band, before the latter can be formed. In figure 2 the signs of this are very clear in the form of little shoulders on the sides of the plateaus in the free energies. The transition rates  $\Gamma_{M',M}$  for the formation of these elliptical shapes will not be proportional to  $B$  but much smaller, since this growth mainly occurs along the short sides of the cluster. The contributions from these terms in the denominator of (2.6) are therefore larger than estimated. Numerically they are important as long as the plateau in the free energy is not too wide. This then will give rise to a notable decrease of the reversal frequencies from our estimated values. Correcting for this in the theoretical expression would require better estimates of  $\Gamma_{M',M}$  in the free energy shoulders, which seem fairly complicated to obtain. Also the growth rates in the magnetization regions beyond the shoulders, where the growing clusters are even smaller, are overestimated by (2.11), but these are weighted less as the free energies there are smaller.

- The above considerations clearly reveal the possibility that the coordinate parametrizing the "reaction path" (here the magnetization) changes non-monotonically along this reaction path; one could imagine that the growing cluster, before turning into a strip, typically decreases in size for a while. In reality this does not seem to happen, but if this were the case, parts of the reaction path with different cluster shape but equal magnetization would be lumped together, and the diffusion process along the cluster size coordinate would no longer correspond to the actual path taken by the cluster. Obviously in such a case the reaction coordinate has to be redefined in such a way that the new coordinate is monotonic along the reaction path indeed. But in complicated situations it may not always be clear what is a proper choice for such a coordinate.
- As a consequence of magnetization fluctuations in the bulk, passages of  $M = 0$  will be registered typically already a short while before the

area between the interfaces reaches the value  $LB/2$  corresponding to an equal division of the system between areas of positive and negative magnetization. The reason is that the typical time scale for fluctuations of the bulk magnetization is much shorter than that for interface diffusion, so for each location of the interfaces the whole range of accessible magnetization values typically will be scanned. Now in most cases this just will give rise to a negligible shift of the time at which the situation of equal areas (this is the physically relevant criterion) is reached, but occasionally it may happen that  $M = 0$  occurs, but the system returns to the pure state it came from without ever reaching equal areas. To check the importance of these events we may compare the average first passage time from  $-M_0$  to  $M_0$  to that from  $\pm M_0$  to  $M = 0$ . If the effect of magnetization fluctuations is negligible the ratio of these should be 2, otherwise it ought to be larger. Note that for the systems considered here the effect of magnetization fluctuations on the first passage time from  $-M_0$  to  $M_0$  is much smaller than that on the first passage time from  $-M_0$  to  $M = 0$ , because the probability of returning to  $-M_0$  without reaching the pure state of positive magnetization, once  $M = M_0$  has been reached, is extremely small. We have measured this ratio for several system sizes and temperatures, excluding those cases where the occurrence of multiple interfaces is likely, and found that the mean value is 1.90, with a standard deviation of 0.15.

- It is of interest to investigate how the reversal times depend on the system size parameters. From (2.6) we may conclude that for long systems (but not so long that multiple interface pairs will occur frequently) the reversal time will become independent of the system length  $L$ . For this one should notice first of all that for  $M$ -values on the plateau  $\exp(\beta F(M))$  is proportional to  $1/L$ , because the number of ways a pair of interfaces may be placed such that the average magnetization equals  $M$ , is proportional to  $L$ . On the other hand the summation over  $M$ , which is dominated by  $M$ -values on the plateau, gives rise to a factor close to  $L$ . Hence to first approximation the reversal frequency  $\nu$  is independent of  $L$ . Remarkably this independence of  $L$  in fact is observed even better by the numerical results than by the theoretical estimates.

In section 2.3.3 it was noted already that the product  $f'$  of the reversal frequency and the Arrhenius factor  $\exp(-\beta F(0))$  depends on  $L$  and  $\beta J$ , but is approximately independent of the system width  $B$ . No-

tice that square systems may be included in this comparison without problem, as the extra factor of 2 due to the two possible orientations of the interfaces, is properly accounted for in the Arrhenius factor.

- We already indicated repeatedly that our theory may be applied only if the probability of having more than two interfaces around the cylinder may be neglected compared to the probability of having just two such interfaces. For this to be case one has to require  $Z_1/Z_0 \ll 1$ . For large enough systems this condition may be rewritten as  $L \ll \exp(\beta\sigma B)$ , with  $\sigma$  the surface tension of the interface. For large systems violation of this condition requires extreme aspect ratios, so under normal conditions it will be satisfied, unless the temperature is very close to the critical one, at which the surface tension vanishes.

## Chapter 3

# Nucleation times

### 3.1 Introduction

Homogeneous nucleation is a prototypic example of escape from a metastable state through thermal activation. In this process a stable nucleus spontaneously grows in a metastable environment. It has been studied extensively, and excellent books and reviews exist [12, 13]. A commonly used system for studying nucleation phenomena is the well-known Ising model. Above the so-called critical temperature, in the absence of an external magnetic field, up- and down-pointing spins are roughly equally abundant. Below the critical temperature, the system prefers to be in either of two states: one state with a positive magnetization, in which most spins are pointing up, and the other state with a negative magnetization. In the presence of a weak external field one of these states is metastable and will decay to the stable equilibrium state through nucleation.

The dynamical and statistical characteristics of this process are the subject of *classical nucleation theory* (CNT), which was founded in the first part of the last century by Volmer and Weber [14], Farkas [15], Becker and Döring [16] and Zeldovich [17], among others. In this theory the process is described as the stochastic growth of a droplet, which may grow or shrink by the attachment or detachment of single molecules. The rates for these elementary processes are assumed to satisfy a detailed balance condition determined by the free energy of the droplet. In its simplest form this free energy consists of the following two contributions: a bulk contribution equal to the number of particles in the cluster times the chemical potential difference between the stable and the metastable state (also called the supersaturation), and a surface contribution equal to the surface area

times the surface tension, which is supposed to be the same as that for coexisting states in equilibrium. The shape of the droplet is assumed to be isotropic (circular in two, spherical in three dimensions). For small droplets the surface term dominates and the droplet free energy increases with size. For large droplets the bulk term dominates. Therefore the free energy as a function of cluster size  $C$ , expressed in the number of molecules within the cluster, goes through a maximum at a critical cluster size  $C_x$ . For small supersaturation, the free energy difference  $\Delta F \equiv F(C_x) - F(0)$  is typically large compared to  $k_B T$ , with  $T$  temperature and  $k_B$  Boltzmann's constant. Therefore nucleation is a thermally activated process and the *nucleation rate*, i.e. the average number of nucleations per units of volume and time is suppressed by an Arrhenius factor  $\exp[-\Delta F/(k_B T)]$ .

Experimentally homogeneous nucleation rates are not easy to measure, but in the literature there are many reports of simulation work in which homogeneous nucleation rates have been computed. Several authors claim good agreement with classical nucleation theory [18, 19, 20], but many authors mention the need for corrections to the CNT-expression for the cluster free energy. Notably, Auer and Frenkel [8] numerically found that the surface tension of a fairly small cluster of solid immersed in the liquid phase of a hard sphere system under metastable conditions, is markedly beyond the macroscopic surface tension of an equilibrium solid-liquid interface at the same temperature. The same had been observed in real experiments on nucleation in colloidal suspensions [21] and similar results were obtained by density functional and similar calculations [22]. For the two-dimensional Ising model Acharrya and Stauffer [23] claim rough agreement with CNT, but require a surface tension that is roughly 4/3 times the macroscopic value. Shneidman, Jackson and Beatty [24] use exact results to estimate the free energy for very small clusters, but for larger ones they use the expression from CNT with a constant shift based on the exact small cluster free energies. Neuhaus and Hager [25] list several finite-size and curvature corrections to the surface tension, but do not evaluate their quantitative importance under specific conditions.

Here we first of all show that for the two-dimensional Ising model under nonconserving dynamics CNT, and specifically the Becker-Döring equations, work very well, provided one uses realistic values for the cluster free energies combined with effective transition rates that are based on global properties of the interface dynamics and that exhibit a proper dependence on cluster size. Under these conditions we find nucleation rates that differ never more than 20% from their theoretical values, although the range of

values found spans over four decades.

In addition we calculate the effects of an initial quench from a high temperature or positive field state into the metastable state. Right after the quench only very small droplets of the stable phase may be found. This first of all gives rise to an asymptotic time shift in the nucleation time distribution, which can be calculated in terms of the parameters of the Becker-Döring equations. This time shift is independent of system size and therefore becomes relatively more important as the system gets larger. Secondly, from the Becker-Döring equations we also obtain the short-time probability distribution function for nucleation after an initial quench, which differs from the Poisson distribution that holds asymptotically for large times (but still small enough that the clusters that have nucleated already, cover only a negligible fraction of the total surface area). Both the asymptotic time shift and the short-time nucleation probability thus obtained show very good agreement to simulation results.

The model that we study is the Ising model on an  $L \times L$  lattice with helical boundary conditions, and non-zero external field. Both the model and the dynamics are described in detail in chapter 1.

The organization of this chapter is as follows. In section 3.2, we outline the theoretical framework and apply it to our model. In section 3.3 we compare the theoretical predictions with the results of high-accuracy computations, and in the final section we discuss our results.

In the previous chapter we applied the same method to estimate the distribution of magnetization reversal times in an Ising model on a finite lattice in the absence of a magnetic field. This is a very similar activated process: the intermediate state of high free energy in this case consists in a state with a strip of opposite magnetization separated from the original bulk state by two straight interfaces. Theoretically this system is somewhat easier to treat, because more is known about straight interfaces in the absence of a field than about the interface between a droplet and the bulk.

## 3.2 Theoretical framework

To study the behavior of nucleation times at temperatures below the critical one we consider an ensemble of systems prepared in configurations with no large negative clusters present (typically by quenching from a positive field equilibrium state). For each system in the ensemble we keep track of the sizes of all of its clusters. These are geometrical clusters, defined as sets of aligned spins, interconnected by bonds between nearest-neighbor sites

and completely surrounded by spins of opposite sign. They are equivalent to Coniglio-Klein clusters [26] in the limit of zero temperature, and do not differ much from these at the temperatures considered here. The sizes of our clusters are defined as the numbers of aligned spins contained in them. We define the nucleation time of a system as the first time at which one of its clusters grows beyond a given size  $A$ , which is comparable to but larger than the critical cluster size for reasons that will be made clear below. For a theoretical description we would like to derive an expression for the probability distribution of the nucleation time under the stochastic dynamics of the system.

The spin-flip dynamics described in section 1.2 may be represented by a master equation for the probability distribution  $P(\mathbf{S}, t)$  of finding a system in the configuration  $\mathbf{S}$  at time  $t$ . Due to the huge number of possible configurations this master equation cannot be solved analytically or even numerically for system sizes of practical interest. Therefore we resort to a couple of approximations that are made standardly in classical nucleation theory. First, we assume that we may treat the clusters of negative spins in the system as being independent. In this approximation, the probability that none of the  $N_c$  clusters has grown beyond the critical size, is simply the  $N_c^{\text{th}}$  power of the probability that a single cluster has not grown beyond the critical size. Secondly, following the Becker-Döring approach [16], we assume that the dynamics of a single cluster may be modeled by a master equation for the probability  $P(C, t)$  that this cluster contains  $C$  spins at time  $t$ :

$$\begin{aligned} \frac{dP(C, t)}{dt} = & \Gamma_{C, C+1}P(C+1, t) + \Gamma_{C, C-1}P(C-1, t) \\ & - (\Gamma_{C+1, C} + \Gamma_{C-1, C})P(C, t), \end{aligned} \quad (3.1)$$

By adopting this equation we make several approximations: we suppress all dependence of the transition rates on the shape of the clusters and we neglect the possibilities of merging or splitting of clusters. In sections 3.3.2 and 3.4 we will come back to this and argue how these effects can be accounted for to a large extent by choosing the transition rates in Eq (3.1) in an appropriate effective way.

In order that the equilibrium distribution of cluster sizes be a stationary solution of the master equation we impose the condition of detailed balance

$$\frac{\Gamma_{C+1, C}}{\Gamma_{C, C+1}} = \exp[\beta(F(C+1) - F(C))], \quad (3.2)$$

where  $\beta F(C) = -\ln[P_{eq}(C)/N]$ , with  $P_{eq}(C)$  the average number of clus-

ters of size  $C$  for a system forced to be in equilibrium in the metastable state (see section 3.3.1). For  $C$  large enough that it is very improbable to find more than one cluster of size  $C$  simultaneously in the metastable system,  $P_{eq}(C)$  may likewise be interpreted as the probability of finding a cluster of size  $C$  in it.

The long-time nucleation rate as predicted by the master equation (3.1) follows as the largest eigenvalue (with a minus sign) of this equation, supplemented with an absorbing boundary at  $C = A$ . Here  $A$  is an integer larger than the critical cluster size  $C_x$ , chosen such that  $P_{eq}(A) \gg P_{eq}(C_x)$ , and clusters with size  $A$  are almost certain to nucleate. The absorbing boundary condition is implemented by setting  $\Gamma_{A-1,A}$  equal to zero.

The largest eigenvalue  $-\nu$  of  $\Gamma_{C,C'}$  in Eq. (3.1), as well as the corresponding eigenvector  $P_0(C)$ , may be found by requiring that the net current away from cluster size  $C$  assumes the value  $\nu P_0(C)$ . Using conservation of probability one easily shows that this may be expressed as

$$\begin{aligned} j_{C+1,C} &\equiv \Gamma_{C+1,C}P_0(C) - \Gamma_{C,C+1}P_0(C+1) \\ &= \nu \sum_{c \leq C} P_0(c), \end{aligned} \quad (3.3)$$

$$\nu = \frac{\Gamma_{A,A-1}P_0(A-1)}{\sum_{c \leq A-1} P_0(c)}, \quad (3.4)$$

where  $j_{C+1,C}$  is defined as the net current flowing from  $C$  to  $C+1$ . This current may be approximated by

$$j_{C+1,C} = \begin{cases} \nu \frac{\sum_{c=1}^C \exp[-\beta F(c)]}{\sum_{c=1}^{C_x} \exp[-\beta F(c)]}, & C \leq C_x \\ \nu, & C \geq C_x \end{cases} \quad (3.5)$$

because the sum on the right-hand side of Eq. (3.3) is dominated by the terms with small  $c$ -values, for which  $P_0(c)$  is approximately proportional to  $\exp[-\beta F(c)]$ . This may be checked in hindsight against the solution obtained. With this approximation the equation may be solved recursively for  $P_0(c)$  in terms of  $P_0(A-1)$  for  $c = A-2, A-3, \dots$ , with the result

$$\frac{P_0(c)}{P_0(A-1)} = \frac{\Gamma_{A,A-1}}{\nu} \sum_{m=c}^{A-1} j_{m+1,m} \frac{\exp[\beta(F(m) - F(c))]}{\Gamma_{m+1,m}}. \quad (3.6)$$

Since the sum over  $m$  is dominated by values close to or larger than the critical cluster size, for which  $j_{m+1,m}$  is approximately equal to  $\nu$ , we may

replace Eq. (3.6) by

$$\frac{P_0(c)}{P_0(A-1)} = \Gamma_{A,A-1} \sum_{m=c}^{A-1} \frac{\exp[\beta(F(m) - F(c))]}{\Gamma_{m+1,m}}. \quad (3.7)$$

Now substituting this into Eq. (3.4) we arrive at the result

$$\nu = \left( \sum_{m=1}^{A-1} \frac{\exp[\beta F(m)]}{\Gamma_{m+1,m}} \sum_{c=1}^{C_x} \exp[-\beta F(c)] \right)^{-1}, \quad (3.8)$$

where we have used the fact that the sum over  $c$  is dominated by small values of  $c$  to extend the sum over  $m$  to  $m = 1$ . The result in Eq. (3.8) is well-known. It is usually derived by considering a state with a stationary current in which mass is inserted at a constant rate on one side (e.g. at  $C = 0$  in our case) and taken out as soon as it reaches the absorbing boundary (see e.g. Ref. [6], section IV E). In that case the replacement of  $j_{m+1,m}$  by a constant is exact.

For arbitrary initial distributions  $P(C, 0)$  that are concentrated near the origin, one may give an even more accurate representation of the long-time behavior of  $P(C, t)$ , by writing it in the form

$$P(C, t) = k P_0(C) \exp[-\nu t] \text{ for } t \rightarrow \infty, \quad (3.9)$$

where  $k$  is a constant which represents the component of  $P(C, 0)$  along  $P_0(C)$  if  $P(C, 0)$  is decomposed in terms of the eigenfunctions of the master equation. This gives for the probability  $S(t)$  that the system has not yet nucleated at time  $t$

$$S(t) = \sum_{C=1}^{A-1} P(C, t) = \exp[-\nu(t - t_d)] \text{ for } t \rightarrow \infty, \quad (3.10)$$

where  $t_d$  is called the delay time. The eigenfunction  $P_0(C)$  was given (with a different normalization) in Eq. (3.6):

$$\begin{aligned} \psi^r(n) &\equiv \frac{\nu}{P_0(A-1)\Gamma_{A,A-1}} P_0(n) \\ &= \sum_{m=n}^{A-1} j_{m+1,m} \frac{\exp[\beta(F(m) - F(n))]}{\Gamma_{m+1,m}}, \end{aligned} \quad (3.11)$$

with  $j_{m+1,m}$  given in Eq. (3.5). As a consequence of the condition of detailed balance, Eq. (3.2), the corresponding left eigenvector is obtained by

multiplying  $\psi^r(n)$  by  $\exp[\beta F(n)]$ , or

$$\tilde{\psi}^l(n) = \sum_{m=n}^{A-1} j_{m+1,m} \frac{\exp[\beta F(m)]}{\Gamma_{m+1,m}}. \quad (3.12)$$

Notice that for small values of  $n$  this is virtually independent of  $n$ , because only the largest  $m$ -values give important contributions to the sum. Using the proper normalization of the leading eigenfunction, and approximating  $P(C, 0)$  by  $\delta_{C,1}$ , one now finds immediately that  $t_d$  follows from

$$\exp[\nu t_d] = \frac{\tilde{\psi}^l(1) \sum_{n=1}^{A-1} \left( \exp[-\beta F(n)] \tilde{\psi}^l(n) \right)}{\sum_{n=1}^{A-1} \left( \exp[-\beta F(n)] \left( \tilde{\psi}^l(n) \right)^2 \right)}. \quad (3.13)$$

Now, by subtracting unity on both sides, dividing by  $\nu$ , approximating sums over  $m$  from  $n$  to  $A-1$  by sums from 1 to  $A-1$ , where appropriate, substituting Eq. (3.12) and using Eq. (3.5) for  $j_{m+1,m}$ , one obtains

$$t_d = \frac{\sum_{n=1}^{A-1} \sum_{m=1}^{n-1} \left( \frac{W(n)}{\Gamma_{m+1,m} W(m)} \sum_{k=1}^{\min[m, C_x]} W(k) \right) \tilde{\psi}^l(n)}{\sum_{n=1}^{A-1} \left( W(n) \tilde{\psi}^l(n) \right)}, \quad (3.14)$$

with  $W(n) \equiv \exp(-\beta F(n))$ .

### 3.3 Simulations and results

For applying the above theoretical framework to nucleation times in the Ising model, the two ingredients required are: (i) the cluster free energies  $F(C)$ ; and (ii) the transition rates  $\Gamma_{C',C}$  from cluster sizes  $C$  to  $C'$ . We obtain these two ingredients via two different computational tools.

In all our simulations, we use a technique known as multispin coding [27], which enables us to reach long simulation times and thus good statistics. All random numbers are generated with a lagged Fibonacci generator, as provided in Ref. [27].

### 3.3.1 Cluster free energies

We measure the distribution of cluster sizes for various values of  $\beta$  and  $h$ , in a system with  $64 \times 64$  spins. We are actually only interested in the distribution of clusters smaller than a certain size  $A$ , which was discussed in section 3.2. Therefore we define a cut-off cluster size  $C_{max}$ , which is typically chosen to be 300. We modify our algorithm in the following way: starting with a configuration  $S_i$  we perform a fixed number  $M$  of Monte Carlo steps, and measure the sizes of all the clusters of down-spins in the system. If there is a cluster with more than  $C_{max}$  spins we reject the new configuration and choose  $S_{i+1} = S_i$ . Otherwise we accept the new configuration as our  $S_{i+1}$ . In all cases we add the sizes of the clusters in  $S_{i+1}$  to a histogram. After many repetitions of this loop we find the free energy  $F(C)$  from

$$\beta F(C) = -\ln \frac{\langle N(C) \rangle}{N} \quad (3.15)$$

where  $\langle N(C) \rangle$  is the average number of clusters of size  $C$  in the system with  $N$  sites.

If  $C_{max}$  is chosen too large, the various clusters in the system influence each other. In particular, excluded volume effects inside and around large clusters suppress larger clusters in the metastable state more than smaller ones. As a consequence the distribution of cluster sizes depends on  $C_{max}$ . To determine whether a certain value of  $C_{max}$  is allowed, we check that the free energy curve coincides with the same curve, obtained with a lower value for  $C_{max}$ .

Figure 3.1 shows our measurements for the free energy according to Eq. (3.15) as a function of cluster size, for some combinations of temperature and external field.

For large clusters, one may expect that classical nucleation theory can be used. At not too low temperature the clusters on average are nearly circular in shape. The free energy is then approximated by the Becker-Döring expression [16]

$$F(C) \approx F_0 + 2\sigma\sqrt{\pi C} - 2hC, \quad (3.16)$$

where  $\sigma$  is the excess free energy of the interface per unit length, and  $h$  the strength of the external field.

Strictly speaking, in order to account correctly for the difference between the free energies of the metastable and the stable phase, one should replace  $2hC$  by  $2hC(2m_s - 1)$ , with  $m_s$  the average spin per lattice site. At the temperatures considered here, however,  $m_s$  is very close to unity, so

this correction is very small. In two dimensions there are also physical contributions to this term, resulting from the Laplace pressure (compression of the cluster under the influence of surface tension) and from Tolman, or curvature corrections [28]. We fitted  $F_0$  and  $\sigma$  to the data in figure 3.1, and added the corresponding curves as lines in the same figure. The measurements are well fitted by the curves, as long as the cluster size is not too small. However, the surface tensions obtained in this way are larger than those given by the Onsager expression [29]

$$\sigma = 2J + \beta^{-1} \ln \tanh \beta J, \quad (3.17)$$

valid for long horizontal or vertical interfaces, and zero external field (see figure 3.2). At the temperatures we considered, the surface tension is known to be almost isotropic [30], so anisotropy effects cannot explain this difference. As suggested by Fig. 3.2 both field dependence of the surface tension and corrections due to the finite size of the clusters may play a role here. Note that similar corrections for the surface tension on a finite cylinder are present already in Onsager's exact solution [29]. For a precise determination of nucleation rates these corrections are quite important. They may easily cause a change by a few orders of magnitude in the values of average nucleation rates.

### 3.3.2 Interface diffusion coefficient

The second ingredient required in the theoretical framework of section 3.2 is the rate  $\Gamma_{C+1,C}$  of cluster growth. To estimate this rate we study the diffusion of a single interface in a system with anti-periodic boundary conditions in the absence of an external field, as described in chapter 2. The location of the interface is obtained from the magnetization  $M$ . The diffusion coefficient  $D$  is defined as:

$$D = \lim_{t \rightarrow \infty} \left[ \frac{\langle (M(t) - M(0))^2 \rangle}{2t} \right]. \quad (3.18)$$

This diffusion coefficient is found, to a good approximation, to depend linearly on the length of the interface  $B$ :

$$D(B, L, \beta J) = g(\beta J)B + c, \quad (3.19)$$

where the constant  $c$  was added to allow for potential finite-size effects. In an appendix we show that such corrections are to be expected indeed, on the basis of a simple model calculation for a 2-dimensional BCSOS

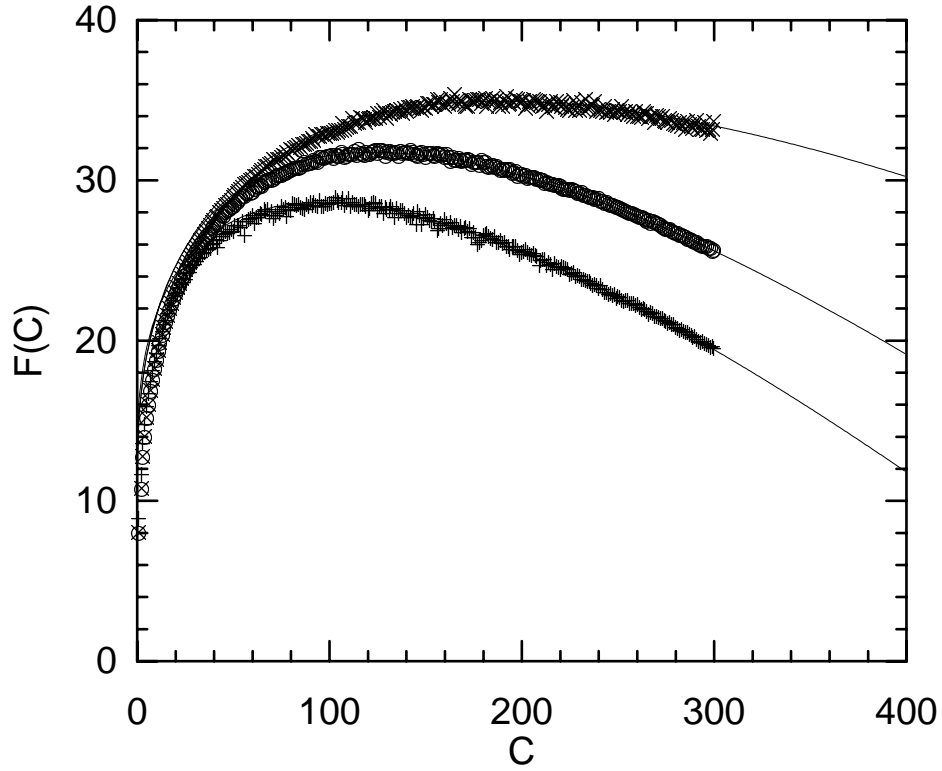


Figure 3.1: Free energy as a function of cluster size in the  $64 \times 64$  system at  $\beta J = 0.56$  and  $h = 0.06$  ( $\times$ ),  $\beta J = 0.58$  and  $h = 0.08$  ( $\circ$ ), and  $\beta J = 0.53$  and  $h = 0.08$  ( $+$ ). The lines represent the Becker-Döring expression Eq. (3.16), with fitted values  $\sigma = 0.93$ ,  $1.00$  and  $0.88$ , and  $F_0 = 12.3$ ,  $11.9$  and  $13.4$ .

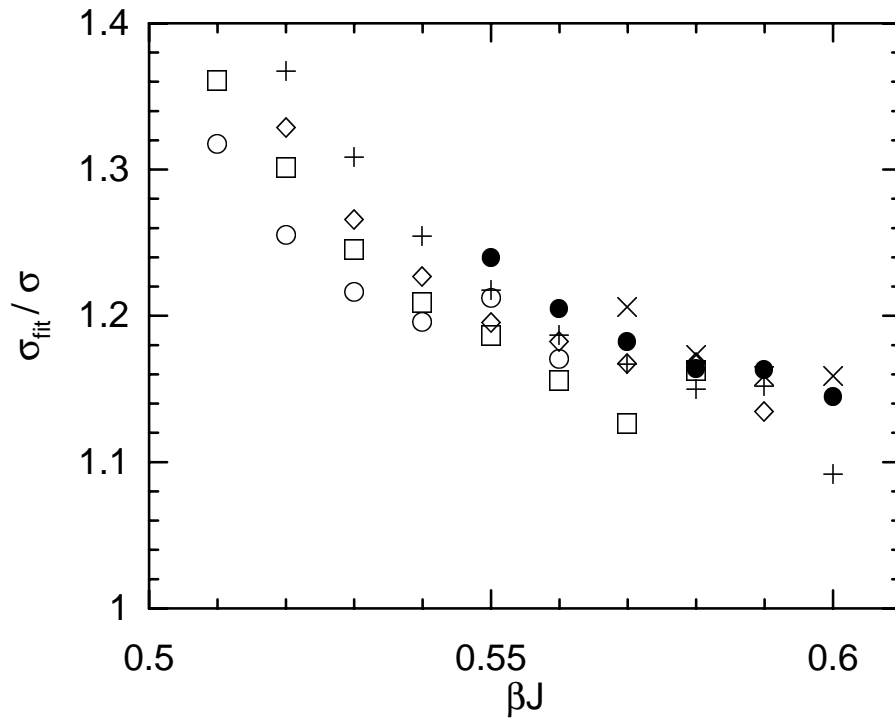


Figure 3.2: Ratio of the surface tension obtained by fitting the free energy curve and the theoretical value given in Eq. (3.17), as a function of  $\beta J$ . Different symbols denote different strengths of the external field:  $h = 0.05$ ( $\circ$ ),  $h = 0.06$ ( $\square$ ),  $h = 0.07$ ( $\diamond$ ),  $h = 0.08$ ( $+$ ),  $h = 0.09$ ( $\bullet$ ) and  $h = 0.10$ ( $\times$ ).

model. One might expect small corrections to Eq. (3.19) due to the helical boundary condition. However, as mentioned already, at the temperatures studied the surface tension is almost perfectly isotropic. Therefore the chief effect of the helical boundary conditions is an extension of the interface length to  $\sqrt{B^2 + 1}$ . The effect of this is exactly compensated by the fact that the relevant motion of the interface is not orthogonal to its average orientation, but under a small angle with it. The results for  $g(\beta, J)$  for various temperatures are plotted in figure 3.3.

To arrive at an estimate for the rates  $\Gamma_{C\pm 1, C}$  for cluster growth and shrinkage, we assume that the diffusion coefficient neither depends on the external field nor on the shape of the interface (straight or circular), but only on the length of the cluster boundary, for which we use  $2\sqrt{\pi C}$ , assuming that the shape of the cluster is almost circular.

This approximation neglects the possibility of having a few positive spins inside the clusters, but at the temperatures studied this will at most amount to a systematic underestimate of the boundary length by a few percent. For large clusters the assumption of circular shape should be very good. From Eqs. (3.8) and (3.14) we see that the contributions from small clusters to the expressions for  $\nu$  and  $t_d$  are almost negligible, and inaccuracy of the estimates of their boundary lengths is not very important. This then gives rise to a jump rate

$$\Gamma_{C+1, C} = \frac{g(\beta J)}{4} 2\sqrt{\pi C}. \quad (3.20)$$

The factor 4 arises because the jumps in magnetization go by units of 2. Alternatively, instead of  $\Gamma_{C+1, C}$  we could have identified  $\Gamma_{C, C+1}$  through  $D$ . The detailed balance condition (3.2) causes these quantities to be slightly different. However, for  $C$ -values close to the free energy maximum, which are weighted most strongly, their difference becomes very small. In addition there will be some compensating effects, because for  $C \geq C_x$  one has  $\Gamma_{C+1, C} > \Gamma_{C, C+1}$  whereas for  $C < C_x$  this is just the other way around.

### 3.3.3 Nucleation rates

To measure nucleation rates, we first bring the system into equilibrium in the presence of a magnetic field. At time  $t = 0$ , we then reverse all the spins (equivalent to an instantaneous reversal of the magnetic field) so that the system is near its metastable equilibrium. We measure the time the system needs to reach the magnetization corresponding to the stable equilibrium.

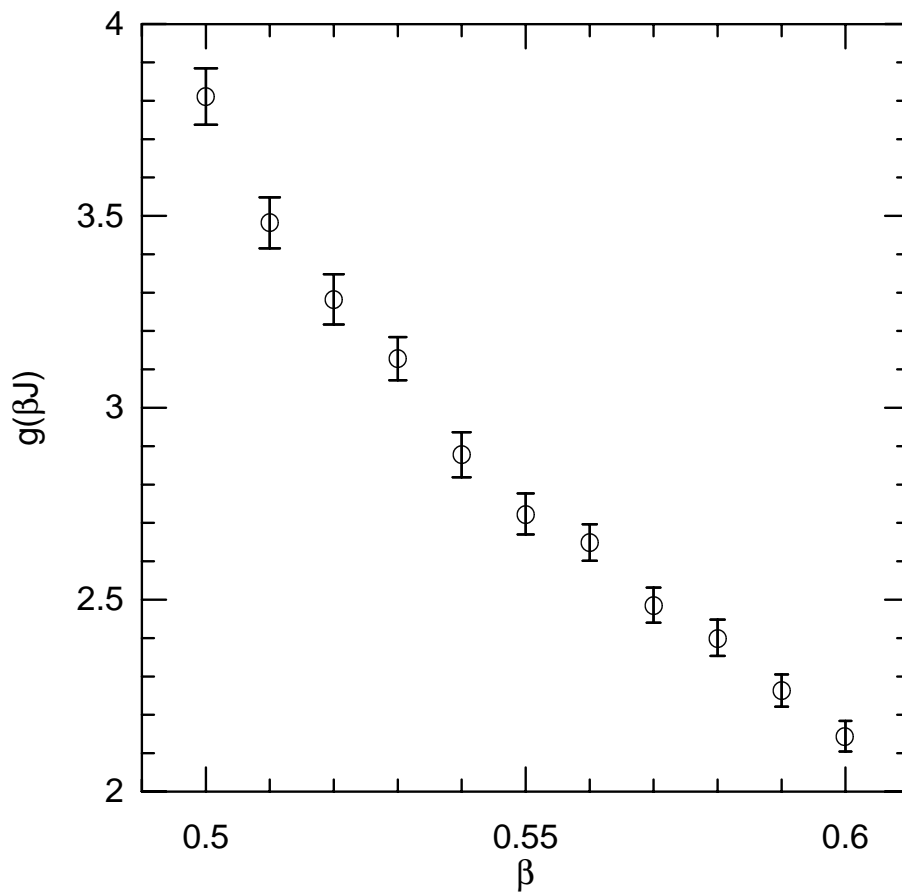


Figure 3.3: Monte Carlo measurements of the diffusion coefficient per interface length  $g(\beta J)$ , as a function of inverse temperature  $\beta J$ .

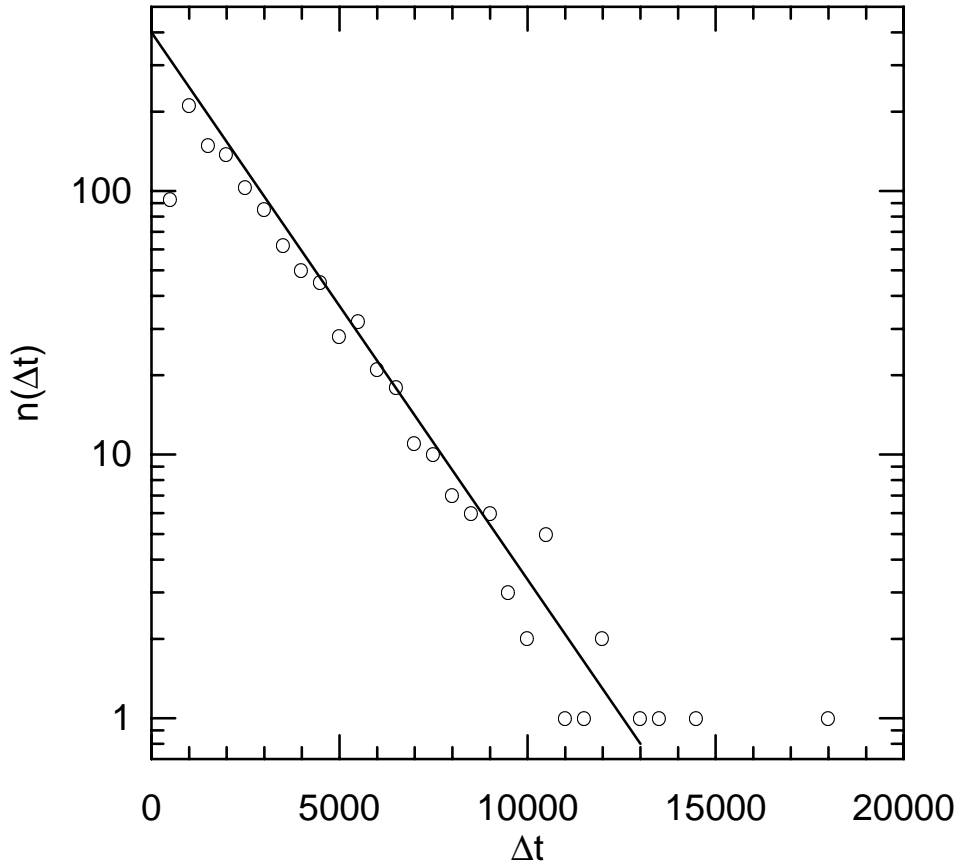


Figure 3.4: Histogram of the number of nucleations as function of the time  $\Delta t$  elapsed before nucleation occurs, at inverse temperature  $\beta J = 0.54$  and external field strength  $h = 0.08$ , in a system with  $64 \times 64$  sites. The straight line is a fit, given by  $n(\Delta t) \sim \exp(\Delta t/1990)$ .

Nucleation has taken place as soon as a cluster has grown well beyond the critical nucleus size. Once that happens, the relatively small systems in our simulations will quickly equilibrate in the state in which most spins align with the external field. Since monitoring the size of the biggest cluster is computationally demanding, we monitor instead the total magnetization, and conclude that nucleation has taken place as soon as it has reached a value corresponding to the stable equilibrium. We make a histogram of all the measured times.

Figure 3.4 shows that at long times the decay function  $f(t)$  behaves

as  $f(t) \sim \exp(-\nu_s t)$ . Here, we focus on the long-time behavior, and are specifically interested in the asymptotic nucleation rate  $\nu_s$ . We obtain this quantity via a fitting procedure, in which we ignore the data up to a time  $t_0$ , chosen such that  $f(t)$  shows exponential time behavior for  $t > t_0$ . Then we determine the time  $t'$  at which half of the remaining events have taken place. We then obtain the first nucleation time  $\tau \equiv \nu_s^{-1}$  from  $\tau = (t' - t_0)/\ln(2)$ . Instead we could have made a linear fit of all the data points beyond  $t_0$ , but this makes no significant difference. Table 3.1 gives the measured first nucleation times  $\tau_1$ . In the same table, we also report the estimated first nucleation times  $\tau_2 = (\langle N_c \rangle \nu)^{-1}$  with  $\nu$  as obtained in Eq. (3.8) and  $\langle N_c \rangle \equiv \sum_{C=1}^A N(C)$  the average number of clusters in the system, as determined from our simulation data. Finally we also give the ratio  $\tau_2/\tau_1$ . The table shows that, while the values of the first nucleation times span four decades in time, the estimated and measured first nucleation times agree mostly within 20%, and in many cases even better.

### 3.3.4 Short-time behavior

Besides the long-time exponential behavior of the first nucleation probability, we also studied the deviations from this behavior at short times. To do so we solved the master equation (3.1) for the time evolution of one cluster numerically, with the initial condition that the cluster consists of a single spin:

$$P(C, 0) = \delta_{C,1}. \quad (3.21)$$

We then computed the cumulative probability distribution  $P_{nuc}(1, t)$  that the cluster has grown beyond a certain size  $C_{max}$  during time  $t$ . The corresponding probability distribution for the nucleation of one of  $N_c$  statistically independent clusters at  $C_{max}$ , at time  $t$ , is given by

$$1 - P_{nuc}(N_c, t) = [1 - P_{nuc}(1, t)]^{N_c}. \quad (3.22)$$

The quantity  $P_{nuc}(N_c, t)$  should be equal to the cumulative distribution of nucleation times, if we define nucleation as the first occurrence of a cluster of  $C_{max}$  spins anywhere in the system.

We have compared this result with the results of direct simulations,  $\beta J = 0.54$  and  $h = 0.08$ , for three different system sizes:  $32 \times 32$ ,  $64 \times 64$ , and  $128 \times 128$ . In all cases the starting configuration was a system in which all spins are antiparallel to the external field. Within a few time steps this develops into a quasi-equilibrium distribution for the small clusters. For the system sizes studied presently typical nucleation times are in the order

Table 3.1: Measured values ( $\tau_1$ ) and estimated values ( $\tau_2$ ) for the nucleation times in the  $64 \times 64$  system.

$\beta J$	$h$	$\tau_1$	$\tau_2$	$\tau_2/\tau_1$
0.51	0.04	$1.83 \times 10^4$	$2.26 \times 10^4$	1.234
0.51	0.05	$3.35 \times 10^3$	$3.84 \times 10^3$	1.146
0.51	0.06	$9.84 \times 10^2$	$1.14 \times 10^3$	1.163
0.52	0.04	$1.07 \times 10^5$	$1.09 \times 10^5$	1.019
0.52	0.05	$1.13 \times 10^4$	$1.31 \times 10^4$	1.153
0.52	0.06	$2.84 \times 10^3$	$3.57 \times 10^3$	1.257
0.52	0.07	$8.51 \times 10^2$	$1.09 \times 10^3$	1.276
0.52	0.08	$3.96 \times 10^2$	$4.49 \times 10^2$	1.134
0.53	0.05	$4.15 \times 10^4$	$4.79 \times 10^4$	1.153
0.53	0.06	$8.94 \times 10^3$	$9.47 \times 10^3$	1.059
0.53	0.07	$2.31 \times 10^3$	$2.57 \times 10^3$	1.111
0.53	0.08	$8.98 \times 10^2$	$9.59 \times 10^2$	1.068
0.54	0.05	$1.73 \times 10^5$	$2.13 \times 10^5$	1.228
0.54	0.06	$2.90 \times 10^4$	$3.11 \times 10^4$	1.071
0.54	0.07	$6.69 \times 10^3$	$7.27 \times 10^3$	1.087
0.54	0.08	$2.17 \times 10^3$	$2.32 \times 10^3$	1.068
0.55	0.05	$8.03 \times 10^5$	$1.13 \times 10^6$	1.410
0.55	0.06	$9.57 \times 10^4$	$1.08 \times 10^5$	1.126
0.55	0.07	$1.97 \times 10^4$	$2.08 \times 10^4$	1.054
0.55	0.08	$5.60 \times 10^3$	$5.98 \times 10^3$	1.070
0.55	0.09	$2.05 \times 10^3$	$2.17 \times 10^3$	1.058
0.56	0.05	$4.02 \times 10^6$	$4.59 \times 10^6$	1.140
0.56	0.06	$3.78 \times 10^5$	$4.17 \times 10^5$	1.103
0.56	0.07	$5.81 \times 10^4$	$6.44 \times 10^4$	1.109
0.56	0.08	$1.48 \times 10^4$	$1.57 \times 10^4$	1.058
0.56	0.09	$4.92 \times 10^3$	$5.11 \times 10^3$	1.038
0.57	0.06	$1.47 \times 10^6$	$1.36 \times 10^6$	0.927
0.57	0.07	$1.84 \times 10^5$	$1.98 \times 10^5$	1.080
0.57	0.08	$4.14 \times 10^4$	$4.40 \times 10^4$	1.062
0.57	0.09	$1.24 \times 10^4$	$1.24 \times 10^4$	1.000
0.57	0.10	$4.02 \times 10^3$	$4.53 \times 10^3$	1.128

Table 3.1 (continued): Measured values ( $\tau_1$ ) and estimated values ( $\tau_2$ ) for the nucleation times in the  $64 \times 64$  system.

$\beta J$	$h$	$\tau_1$	$\tau_2$	$\tau_2/\tau_1$
0.58	0.06	$5.80 \times 10^6$	$6.60 \times 10^6$	1.139
0.58	0.07	$6.18 \times 10^5$	$5.72 \times 10^5$	0.926
0.58	0.08	$1.10 \times 10^5$	$1.26 \times 10^5$	1.143
0.58	0.09	$3.06 \times 10^4$	$3.11 \times 10^4$	1.015
0.58	0.10	$1.13 \times 10^4$	$1.06 \times 10^4$	0.938
0.59	0.07	$2.25 \times 10^6$	$2.48 \times 10^6$	1.104
0.59	0.08	$3.49 \times 10^5$	$4.22 \times 10^5$	1.209
0.59	0.09	$8.47 \times 10^4$	$8.36 \times 10^4$	0.987
0.59	0.10	$2.31 \times 10^4$	$2.47 \times 10^4$	1.068
0.60	0.08	$1.04 \times 10^6$	$1.19 \times 10^6$	1.145
0.60	0.09	$2.05 \times 10^5$	$2.52 \times 10^5$	1.229
0.60	0.10	$5.81 \times 10^4$	$6.72 \times 10^4$	1.156

of a hundred time steps, so the fact that we started from clusters of size zero rather than unity makes no real difference. Figure 3.5 shows the results. Here the parameter  $N_c$  was determined in the same simulations that were used to obtain the free energy as a function of cluster size.

The asymptotic slopes of the curves in the top panel of figure 3.5 correspond to the nucleation rates. The times at which straight-line fits to these curves cross  $1 - P_{nuc} = 1$  correspond to the waiting times  $t_d$ , as introduced in Eq. (3.10). There is excellent agreement between the direct simulations and the parameter-free theoretical framework: The theoretical prediction obtained with Eq. (3.14) is  $t_d = 234$  MC time units, while the fits vary between  $t_d = 228$  and  $239$  MC time units. Also the behavior at short times is well described by the theoretical framework, as is evidenced in the bottom panel of figure 3.5.

It is of interest to compare  $t_d$  to the lag time introduced in Ref. [20]. This lag time describes the delay with respect to the inverse nucleation frequency in the average time for observing for the first time a cluster of radius  $R$ . Like our  $t_d$  it is independent of system size, but in contrast to this it strongly depends on  $R$ ; the expression given for it in Ref. [20] even diverges at the critical cluster radius.

The comparison of nucleation probabilities at late times was discussed in the preceding subsection.

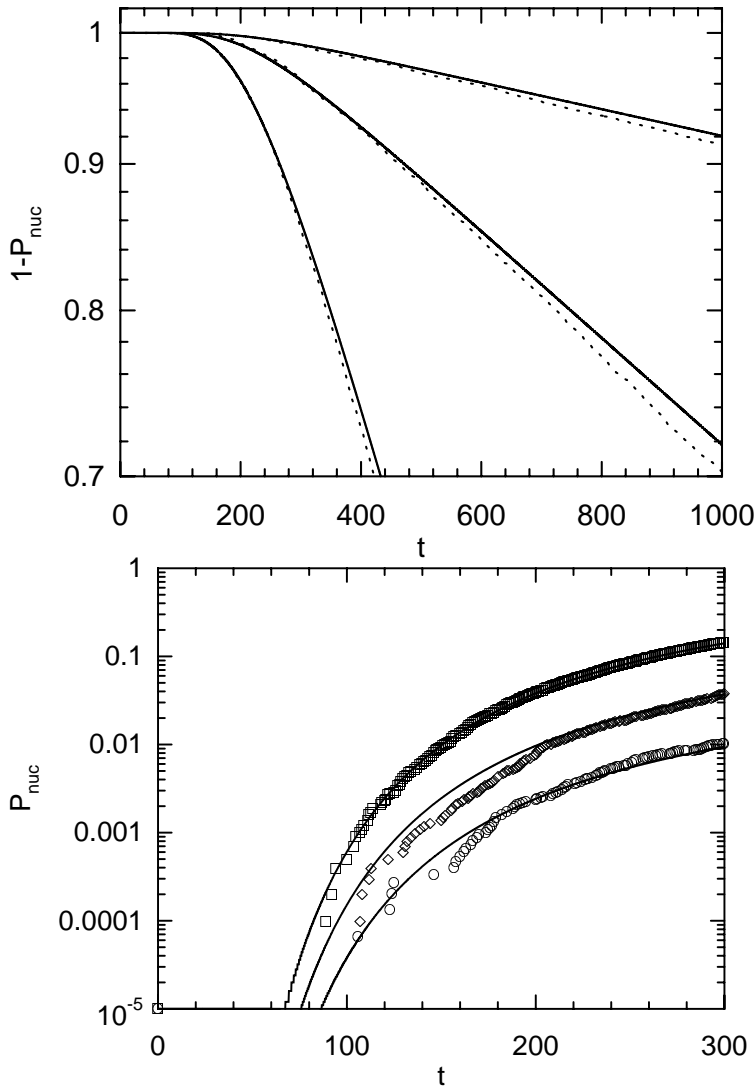


Figure 3.5:  $1 - P_{nuc}(t)$  obtained from the time evolution of one cluster (solid lines) according to the master equation (3.1) combined with Eq. (3.22), and by direct simulation of systems with  $32 \times 32$ ,  $64 \times 64$ , and  $128 \times 128$  spins (the dotted lines) at  $\beta J = 0.54$  and  $h = 0.08$ . In both cases, the highest of the three curves corresponds to the smallest system, and the lowest one to the largest system. The lower plot shows the same data, but focuses on short times.

### 3.4 Discussion

In this chapter we showed that for two-dimensional Ising models with spin-flip dynamics classical nucleation theory provides an excellent description of nucleation time distributions, provided a realistic description is used for the free energy of the growing droplets. We determined this free energy from cluster size distributions in equilibrium Monte Carlo simulations and found that it may be fitted well by the Becker-Döring expression, provided one uses surface tensions that are 10 to 20% higher than the surface tension of a bulk interface at zero field. Similar conclusions were reached by Auer and Frenkel[8] in their studies of crystal nucleation in colloidal hard sphere systems. They also determined cluster free energies by monitoring the frequency of occurrence of clusters of a given size. Like us they could fit the resulting curves quite well by a Becker-Döring expression, with an effective surface tension. In their case the excess over the bulk surface tension at zero supersaturation is about 20 to 40%. They attribute the difference to a density (or chemical potential) dependence of the interfacial tension between the metastable and the stable state. In our case this corresponds to a magnetic field dependence. In fig. 3.2 we see that such a dependence indeed seems to be present in our system, but quite definitely there are other corrections, due to finite cluster size, and there must also be size independent Gibbs-Thompson and Tolman corrections.

A point one may question is whether the assumption of independent noninteracting clusters holds even for clusters of small size. This may indeed be doubted, but fortunately, at least for the asymptotic nucleation frequency  $\langle \nu N_c \rangle$  this is not really relevant. One may choose to define as clusters only those clusters that have a size  $c \geq m_0$ , with  $m_0$  chosen such that clusters of this size already are very rare, but still  $\exp(\beta F(m_0)) \ll \exp(\beta F(C_x))$ . From Eqs. (3.8) and (3.15) it then follows that

$$\nu_{m_0} = \frac{\sum_{c=1}^{C_x} N_c}{\sum_{c=m_0}^{C_x} N_c} \nu,$$

since the terms with  $m < m_0$  in the first sum in Eq. (3.8) basically do not contribute. As a consequence of this the asymptotic nucleation rate in the system is independent of the choice of  $m_0$ .

For the short-time nucleation rate the free energy of small clusters is important indeed, especially if one starts from a state of zero magnetization. However, if one starts from a quasi-equilibrium distribution representing the state after a sudden reversal of the magnetic field, the short-time behavior will be dominated by clusters that were fairly large at the outset

and again Eq. (3.15) may be trusted. In [31] Van Beijeren gave explicit expressions for the short-time behavior, which may be used if the latter is well approximated by a diffusion equation in an external potential. In the present case these cannot be used, since on the relevant time scales the hopping process between neighboring cluster sizes is not well-approximated by a diffusion process. And since the hopping rates depend on cluster size no analytic expressions for the short-time behavior are available. But the numerical solution of the master equation (3.1) gives a very good agreement with the results from our Monte Carlo simulation of the nucleation process, as was shown in Fig. 3.5.

Besides the free energy as a function of cluster size our calculations require the transition rates  $\Gamma_{C,C\pm 1}$  between neighboring values of the cluster size. These we estimated by setting them proportional to the mean circumference of a cluster, determining the proportionality constant from the simulated mobility of a straight interface in cylindrical geometry and imposing the detailed balance condition (3.2).

In our estimations we have been using a number of assumptions, whose validity is not guaranteed under all conditions:

- Strong fields should modify the diffusion coefficient; this effect is neglected. The freedom to modify the field strength within the metastable region is limited though, and long nucleation times, as seen mostly in real experiments, require weak fields.
- The diffusion coefficient is assumed to be determined by the size of the cluster alone, and is calculated on the assumption that its shape is strictly spherical. This requires that the temperature is not too low, because at very low temperatures the equilibrium shape of the cluster is more square than circular [30]. (This however, is an effect that may easily be corrected for without making any basic changes in the theory.) On the other hand the temperature should not be too close to the critical temperature for shape fluctuations to be reasonably small. To some extent these fluctuations are taken into account, since our calculation of the diffusion coefficient is done for a fluctuating interface around a cylinder. But it is by no means certain that the fluctuations of a circular interface are in all aspects comparable to those of the interface around the cylinder.
- It may happen that a cluster splits up or that two clusters merge, corresponding in our theoretical framework to non-zero transition rates  $\Gamma_{C,C+i}$  and  $\Gamma_{C+i,C}$  with  $i > 1$ . This effect also is partly accounted for

through the numerical determination of the diffusion constant on a cylinder, but especially for larger clusters the difference in geometry may cause additional effects. However, these will only become important in systems that contain a sizable density of clusters of spins aligned with the external field. Hence, also this approximation can be trusted least near the critical point.

- No memory effects are accounted for explicitly. For spin-flip dynamics, memory effects will chiefly be due to the influence of shape fluctuations on the transition rates. Since shape fluctuations on larger length scales will decay only slowly, these may be fairly long lasting effects. Again, our way of determining the diffusion coefficient will take many of these effects into account implicitly, but memory effects involving large shape fluctuations may be different for the present cluster geometry. For magnetization conserving dynamics (consisting e.g. of local spin exchanges) much stronger memory effects exist due e.g. to the effect that a spin that is released from a large cluster has high probability of reattaching to it soon.

Under conditions in which the effects above are negligible, our theoretical framework is capable of estimating nucleation rates with an accuracy in the range of 20%. The small systematic overestimation by about 10% of the nucleation time by theory may have several causes. The radius of a cluster will be slightly larger than our estimate because especially a large cluster will typically contain a few holes in its interior. Since the equilibrium magnetization is always larger than 0.92 for the temperatures studied, the density of vacancies in the cluster is less than 4%, and hence the increase in interface length due to holes is less than 2%. Also the assumptions that the diffusion coefficient is independent of the magnetic field and of the orientation of the interface may be not entirely correct. At low temperatures a diagonal interface is much more mobile than a straight one, but at the fairly elevated temperatures studied here one would not expect a large orientation dependence. Further there could be effects from the possibility of cluster splittings and mergings, though some of these are accounted for through our numerical determination of the diffusion constant on a cylinder.

## Appendix

To illustrate the dependence of the interface diffusion coefficient on the system size and on the type of boundary conditions, as discussed in sec-

tion 3.3.2, we consider diffusion in a two-dimensional BCSOS model with stochastic dynamics. This model is much simpler than the Ising model and allows for an explicit determination of the diffusion constant as a function of system size and helicity conditions. It is illustrated in Fig. 3.6:

An interface consists of a sequence of straight segments with unit length, oriented with an angle of  $+45^\circ$  (or “up”) or  $-45^\circ$  (or “down”) with respect to the horizontal axis; it separates a completely filled crystal phase from a completely empty vacuum. The interface dynamics consists of evaporation of crystal sites at “peak sites” (consecutive segments oriented up and down) and the deposition of such units at “valley sites” (consecutive segments oriented down and up). When the rates of evaporation and of deposition are equal, the interface performs normal diffusion in the vertical direction, corresponding to a diffusive time evolution of the total mass below the interface. The diffusion constant for this process is easily seen to be equal to the average number of peaks (equal to the number of valleys) in the interface. The determination of this number in equilibrium is a simple combinatorial problem. However, one should treat the boundary conditions properly. In the case of periodic boundary conditions in the horizontal direction, the total numbers of segments up and down have to be equal. Helical boundary conditions may be imposed by requiring  $m$  segments up and  $n$  segments down, with  $m \neq n$ ; we will call these boundary conditions  $(m, n)$ . The equilibrium distribution assigns equal weights to all configurations with the proper values of  $m$  and  $n$ ; one easily sees that this satisfies the detailed balance conditions for the chosen jump rates. The diffusion coefficient may now be expressed as

$$D(m, n) = \Gamma n_g(n, m), \quad (3.23)$$

with  $\Gamma$  the rate of evaporation and deposition, and  $n_g(n, m)$  the average number of peak sites or valley sites in the system. For  $n_g(n, m)$  a simple recursion relation is obtained through the following reasoning: all configurations with boundary conditions  $(m, n)$  may be constructed from all configurations with  $(m, n - 1)$  by adding a down segment at the position just following one of the  $m$  up segments. (In fact each new configuration is obtained precisely  $m$  times this way, but that does not change the reasoning.) If the segment is added at the end of a cluster of up segments it does not increase the number of peaks. On average there are  $n_g(n - 1, m)$  positions where this will happen. In all other cases the number of peaks is

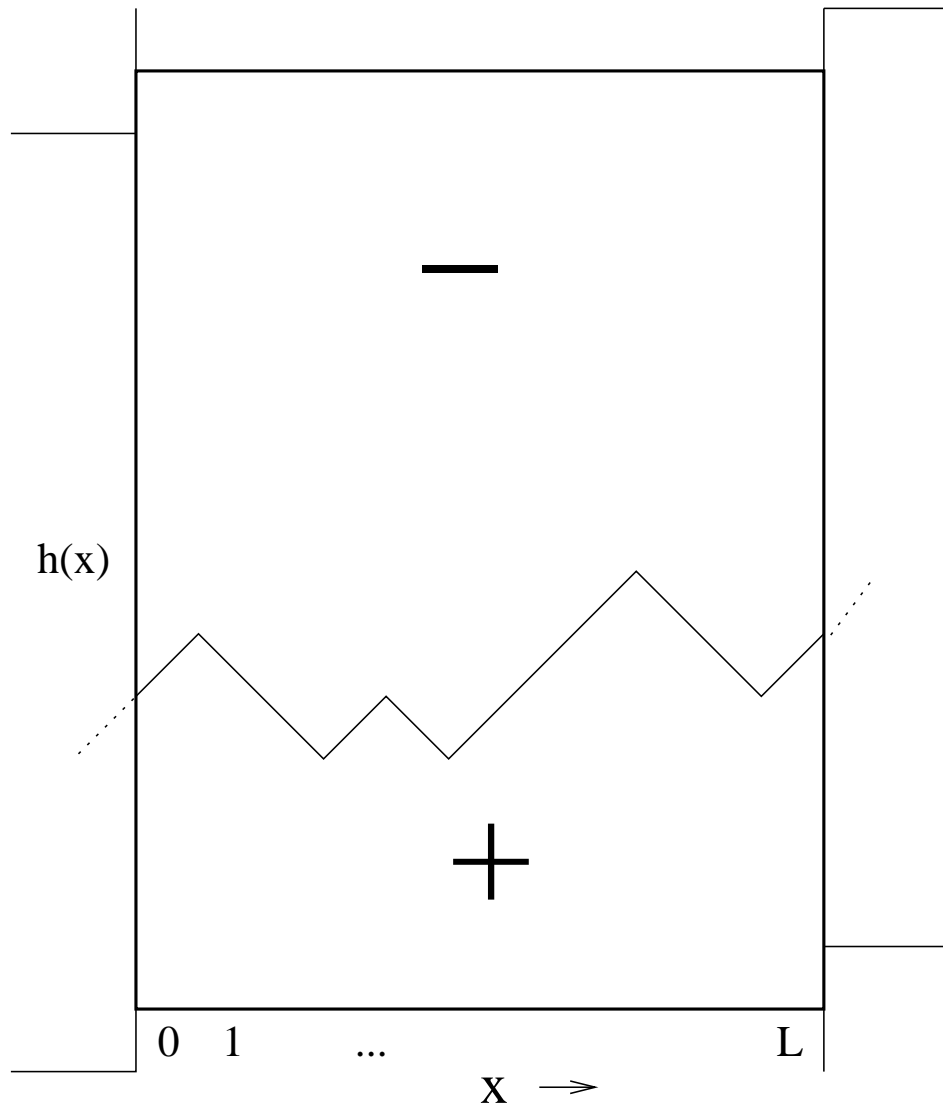


Figure 3.6: Example of an interface configuration in the two-dimensional BCSOS model, with horizontally helical and vertically antiperiodic boundary conditions.

increased by one. As a result one obtains the recursion relation

$$\begin{aligned} n_g(n, m) &= n_g(n-1, m) + 1 - \frac{n_g(n-1, m)}{m} \\ &= 1 + \frac{m-1}{m} n_g(n-1, m). \end{aligned} \quad (3.24)$$

One easily finds that this recursion relation is solved by

$$n_g(n, m) = m \left( 1 - \left( \frac{m-1}{m} \right)^n \right). \quad (3.25)$$

When  $m$  is large this yields

$$n_g(n, m) = m \left( 1 - \frac{1}{e} \right) + \frac{1}{2e},$$

for periodic boundary conditions ( $n = m$ ), and

$$n_g(n, m) = m \left( 1 - \frac{1}{e} \right) - \frac{1}{2e}$$

for helical boundary conditions with  $n = m \pm 1$ . For the Ising model these results can be applied directly to the case of sloped boundaries at very low temperatures, but for higher temperatures calculations would become much harder. Our main point here is to show that generically a constant term is to be expected in Eq. (3.19), in addition to a linear one.

## Chapter 4

# Mass fluctuations of a nucleating droplet

### 4.1 Introduction

#### 4.1.1 Classical nucleation theory

Homogeneous nucleation is a prototypic example of escape from a metastable state through thermal activation. In this process a stable nucleus spontaneously grows in a metastable environment. The dynamical and statistical characteristics of this process are the subject of *classical nucleation theory* (CNT). For a description of CNT, as well as references to reviews on nucleation, we refer to chapter 3.

Classical nucleation theory as described in chapter 3 studies a dynamical process, nucleation, using as input only equilibrium properties, supersaturation and surface tension. Already for this reason, CNT is limited to qualitative or at best semiquantitative statements, like the decrease or increase of the nucleation time with increasing or decreasing supersaturation or surface tension. Quantitative predictions require also some dynamical input into the theoretical framework.

In chapter 3 the description of the free energy as a function of cluster size used as equilibrium input parameters the standard bulk term and a fitted effective surface tension, which generally was 10% to 20% larger than its value in the thermodynamic limit and in absence of an external field. For the dynamics, we used as additional input the diffusion rate of a straight interface separating the two stable phases, in the absence of a driving external field, combined with the assumption that the rate of growth or

shrinkage of a droplet scales linearly with its circumference, approximately proportional to its mass to the power  $1/2$ . This allowed us to predict nucleation times, spanning more than three orders of magnitude, within 20% accuracy, without a fitting parameter.

The previous work left unanswered the physical cause of the higher surface tension. In simulations of hard-sphere colloids Auer and Frenkel [8] also observed a markedly increased surface tension, and suggested that this increase might be an effect of density (or chemical potential) dependence of the interfacial tension between the metastable and the possible stable state, which in our case would correspond to a magnetic field dependence. As alternative causes for the increased surface tension we mentioned finite-size effects, as well as Gibbs-Thomson and Tolman corrections (which in leading order only give a constant contribution to the free energy). Here we come back to this issue, specifically finite-size effects.

Secondly, we address the size-dependence of the rates of cluster growth and shrinkage, as a function of droplet mass. Our approach is to describe the variations in time of the droplet mass by means of the Fokker-Planck equation, with mass-dependent velocity and diffusion coefficient.

The organization of this chapter is as follows: first section 4.1.2 gives a detailed description of the model used in our simulations of nucleation. This is followed in section 4.2 by a discussion of the discretized Fokker-Planck equation whose parameters we fitted to the measured time-evolution of the droplet mass. Next, we present our results in section 4.3, and summarize our findings and draw conclusions in section 4.5.

### 4.1.2 Detailed description of the model

Our simulations of nucleation are performed on the Ising model on a square lattice with lateral dimension  $L$ , which was chosen to be 64, periodic (helical) boundary conditions, and an external magnetic field  $h$  which favors downward-pointing spins. The Hamiltonian of this model reads

$$H = -J \sum_{\langle i,j \rangle} s_i s_j + h \sum_i s_i, \quad (4.1)$$

in which  $s_i = \pm 1$  is the spin at site  $i$ , and  $J$  is the coupling constant. The first summation runs over all pairs of nearest-neighbor sites; under our helical boundary conditions the neighbors of site  $i$  are  $j = i \pm 1$  modulo  $N$  and  $j = i \pm L$  modulo  $N$ , with  $N = L^2$ . Note that in the sum each pair is counted only once. The magnetization is defined as  $M \equiv \sum_i s_i$ ; it can take values  $M = -N, -N + 2, \dots, N$ . We restrict ourselves to systems in which

$L$  is even. As a consequence,  $M$  takes only even values, and summations over a range of possible magnetizations only run over even numbers, with an increment of 2.

The time-evolution is single-spin-flip dynamics with Metropolis acceptance probabilities [10]. If  $S_i$  is the configuration after  $i$  proposed spin flips, a trial configuration  $S'_{i+1}$  is generated by flipping a single spin at a random site. This trial configuration is then either accepted ( $S_{i+1} = S'_{i+1}$ ) or rejected ( $S_{i+1} = S_i$ ); the acceptance probability is given by

$$P_a = \min [1, \exp(-\beta \{E(S'_{i+1}) - E(S_i)\})], \quad (4.2)$$

in which  $\beta = 1/(k_B T)$ . Our unit of time is one Monte Carlo step per particle, so in one unit of time  $N$  Monte Carlo steps are performed and *on average* one spin flip is tried for each site.

In our simulations, we measure at regular intervals the mass of the biggest droplet; here, droplets are geometrical clusters, defined as sets of aligned spins, interconnected by bonds between nearest-neighbor sites and completely surrounded by spins of opposite sign. We restrict ourselves to configurations in which there is no cluster larger than a cut-off cluster size  $C_{max}$ , which we have chosen to be 300. Therefore we modify our algorithm in the following way: starting with a configuration  $S_i$  we perform a fixed number  $M$  of Monte Carlo steps, and measure the sizes of all the clusters of down-spins in the system. If there is a cluster with more than  $C_{max}$  spins we reject the new configuration and choose  $S_{i+1} = S_i$ . Otherwise we accept the new configuration as our  $S_{i+1}$ . In all cases we add the sizes of the clusters in  $S_{i+1}$  to a histogram.

After many repetitions of this loop we find the free energy  $F(C)$  from

$$\beta F(C) = \log(H(C)) - \log \left( \sum_{C'} H(C') \right), \quad (4.3)$$

in which  $H(C)$  is the number of entries of cluster size  $C$  in the histogram.

The aim of our work is to describe the time-evolution of this mass in a quantitative way. In CNT, it is expected to consist of stochastic fluctuations due to the attachment and detachment of spins, biased by the combined effect of the surface tension and the external field.

## 4.2 Fokker-Planck approach

One of the simplest equations that can be used to describe stochastic dynamics is the Fokker-Planck equation:

$$\frac{\partial \rho}{\partial t} = -\frac{\partial}{\partial x}(v\rho) + \frac{1}{2} \frac{\partial^2}{\partial x^2}(D\rho); \quad (4.4)$$

in our case,  $t$  is the time,  $x$  is the mass of the nucleating droplet,  $\rho(x, t)$  is the probability density as function of  $x$  and time  $t$ , and  $v(x)$  and  $D(x)$  are the  $x$ -dependent average velocity and diffusion coefficient, respectively.

We start with a discretized version of the Fokker-Planck equation. After discretizing space and time in units of  $\Delta x$  and  $\Delta t$ , respectively, and neglecting the effects of the boundaries  $i = 0$  and  $i = C_{max}$ , one can approximate it as

$$\begin{aligned} \frac{\rho_i(t + \Delta t) - \rho_i(t)}{\Delta t} = & -\frac{v_{i+1}\rho_{i+1}(t) - v_{i-1}\rho_{i-1}(t)}{2\Delta x} \\ & + \frac{D_{i+1}\rho_{i+1}(t) + D_{i-1}\rho_{i-1}(t) - 2D_i\rho_i(t)}{2(\Delta x)^2}. \end{aligned} \quad (4.5)$$

We can rewrite this equation in matrix form as

$$\rho_i(t + \Delta t) = \sum_j (\delta_{ij} + \Delta t M_{ij}) \rho_j(t), \quad (4.6)$$

where is  $M$  a tridiagonal matrix with elements (again neglecting boundary effects)

$$\begin{aligned} M_{i,i-1} &= \frac{v_{i-1}}{2\Delta x} + \frac{D_{i-1}}{2(\Delta x)^2} \\ M_{i,i} &= -\frac{D_i}{(\Delta x)^2} \\ M_{i,i+1} &= -\frac{v_{i+1}}{2\Delta x} + \frac{D_{i+1}}{2(\Delta x)^2}. \end{aligned} \quad (4.7)$$

Equivalently, we obtain

$$\begin{aligned} v_i &= (M_{i+1,i} - M_{i-1,i}) \Delta x; \\ D_i &= (M_{i+1,i} + M_{i-1,i}) (\Delta x)^2. \end{aligned} \quad (4.8)$$

Note that each column of  $M$  sums to zero; this leaves two free parameters per spatial interval, exactly as many as the parameters  $v_i$  and  $D_i$  in the Fokker-Planck equation.

To determine the effective position-dependent velocity and diffusion coefficient, one may start by constructing a (full) matrix  $T$ , in which element  $T_{i,j}$  contains the frequency with which a droplet of size  $j$  at some time  $t$  has size  $i$  at time  $t + \tau$ , where  $\tau$  is chosen larger than the correlation time between size jumps. The leading eigenvector  $p_i$  of this matrix  $T$  has an eigenvalue of 1, and physically corresponds to the stationary distribution: element  $p_i$  is the probability that the droplet has size  $i$ . Because of detailed balance the eigenvector  $p_i$  satisfies:

$$\frac{p_i}{p_j} = \frac{T_{i,j}}{T_{j,i}}. \quad (4.9)$$

Our assumption is that, effectively, for long times  $\tau$ , the process can be described by eq. (4.6), with  $\Delta t$  approaching zero. The corresponding prediction for transitions from position  $i$  to  $j$  over a time difference of  $\tau \gg \Delta t$  is then

$$\tilde{T} = (I + \Delta t M)^{\tau/\Delta t}. \quad (4.10)$$

Approximately half of the free parameters in the tridiagonal matrix  $M$  are fixed by demanding that  $p_i$  is also an eigenvector of  $M$ , with zero eigenvalue, or equivalently, that  $M$  satisfies detailed balance:

$$\frac{M_{i,i+1}}{M_{i+1,i}} = \frac{p_i}{p_{i+1}}. \quad (4.11)$$

The task at hand is to find the remaining variables in  $M$ , constrained to be norm-conserving, which will yield the best fit between the full matrices  $\tilde{T}$  and  $T$ .

A naive approach would be to express the matrix  $T$  in the basis of its eigenvectors, raise all eigenvalues to the power  $\Delta t/\tau$ , and transform it back to the original basis. In practice, this does not work. The eigenvectors of  $T$  with strongly negative eigenvalues correspond to quickly decaying states and are thus very noisy. However, even such eigenvalues become significant when raised to the small power  $\Delta t/\tau \sim 1/100$ , and thus contribute significantly to  $M$ . Therefore, we take a different approach. With fitting parameters  $M_{i+1,i}$  and  $M_{i,i+1}$  fixed by detailed balance and  $M_{i,i}$  by norm conservation, we perform a minimization of  $\|T - (I + \Delta t M)^{\tau/\Delta t}\|$ . This is implemented by using the routine E04FCF of the NAG library.

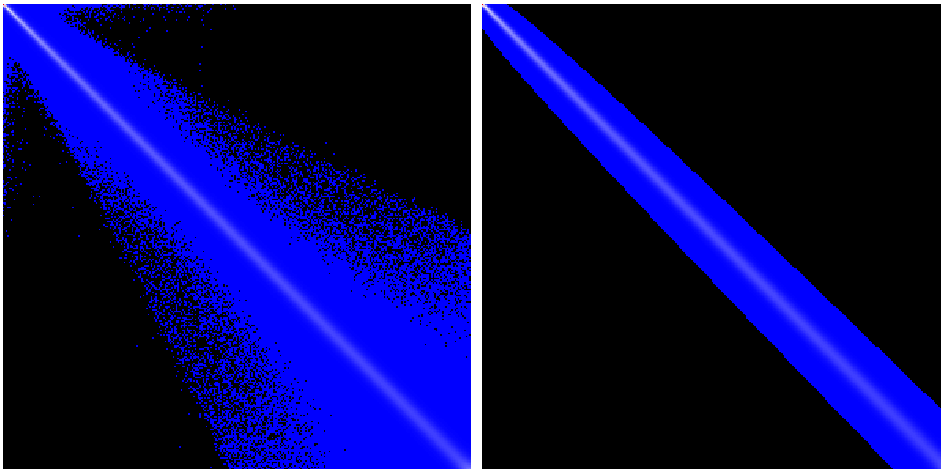


Figure 4.1: Left: the transition matrix  $T$ , from simulations at  $\beta J = 0.54$  and  $h = 0.08$ . Right: the approximate transition matrix  $\tilde{T}$  obtained from a tridiagonal matrix  $M$  raised to the power  $\tau/\Delta t$ . The upper left corner corresponds to clusters of size 4 and the lower right corner to clusters of size 300. The colour scale runs from black ( $= 0$ ), then gradually from blue to white ( $= 0.5$ ), then from white to red ( $= 1$ ).

### 4.3 Simulation results for the cluster free energies

First, we perform long simulations in which we identify the nucleating droplets, correlated over a small time interval  $\tau$ , for which we chose  $\tau = 1/4$ ; we verified that longer time intervals do not yield different results, apart from being more noisy. Based on these data, we fill  $T$ . An example is shown in figure 4.1. We then perform the fitting procedure outlined above, to obtain the tridiagonal transition matrix  $M$ , with  $\Delta t = \tau/100$ . In the right panel of figure 4.1, we have also plotted  $\tilde{T}$  which is obtained from  $M$  according to eq. (4.10). The clear similarity between the two matrices in the vicinity of the diagonal (away from the diagonal the matrix elements are very small) indicates that the approximation of the complicated dynamics of a nucleating droplet by the Fokker-Planck equation is reasonable.

From our result for  $T$  we can find both the equilibrium distribution and the rates of growth and shrinkage of clusters. First, we investigate the leading eigenvector of  $T$ . The components of this eigenvector are proportional to the average density  $p(C)$  of islands of size  $C$ .

The free energy of an island of size  $C$  is written in CNT as

$$r(C) \equiv -\frac{1}{\beta} \ln p(C) = F_0 + 2\sigma \sqrt{\frac{\pi C}{1 - \rho_{st}}} - \frac{2hC(1 - \rho_{st} - \rho_{mst})}{1 - \rho_{st}}, \quad (4.12)$$

with surface tension  $\sigma$ . In this equation  $\rho_{st}$  is the vacancy density in the stable state and  $\rho_{mst}$  the density in the metastable state. The vacancy density  $\rho_{st}$  is, according to the Onsager solution of the Ising model [29], with an extra factor for the external field, given to a good approximation by

$$\rho_{st} = \frac{1}{2} \left( 1 - (1 - \sinh^{-4}(2\beta J))^{\frac{1}{8}} \right) \exp(-2\beta h). \quad (4.13)$$

The value of the free energy offset  $F_0$  in Eq. (4.12) is irrelevant. We set it by the demand that the sum of all probabilities is unity. In CNT, finite-size effects on the surface tension are neglected. As is shown in the appendix, finite-size effects arise, among other effects, from the demand of closure of the droplet if one walks around it. Taking into account only this correction one obtains an effective surface tension behaving for large cluster size as

$$\sigma_{\text{eff}} = \sigma_{\infty} + \frac{3}{4\beta} \sqrt{\frac{1 - \rho_{st}}{\pi C}} \ln C + \mathcal{O}(C^{-1/2}). \quad (4.14)$$

Figure 4.2 shows the measured free energy  $F(C)$  as a function of cluster size  $C$ , at fixed temperature  $\beta J = 0.54$ , and field strengths of  $h = 0.04$  up to  $h = 0.08$ . There is a good agreement between the parameter-free theoretical prediction and the measured data, especially at low field strengths. The larger discrepancies at stronger field strengths can be due to many effects, for instance corrections of the order of  $C^{-1/2}$ , corrections due to the Laplace pressure (estimated as  $C^0$ ), or Tolman contributions to the surface tension.

Figure 4.3 shows the measured free energy  $F(C)$  as a function of cluster size  $C$ , at a fixed strength of the external field  $h = 0.08$ , and temperatures ranging from  $\beta J = 0.5$  to  $\beta J = 0.58$ . Far from the critical temperature, there is an excellent agreement between the parameter-free theoretical prediction and the measured data. Closer to the critical temperature, the agreement is less satisfactory. We contribute this to consequences of the increasing correlation length, of the rapidly increasing density of vacancies in the cluster, and possibly other effects.

Interestingly, the fits improve markedly if a fitted prefactor for the logarithmic correction to the surface tension is allowed (i.e. the second term in Eq. (4.14)). However, we could not find a physical justification for such a prefactor.

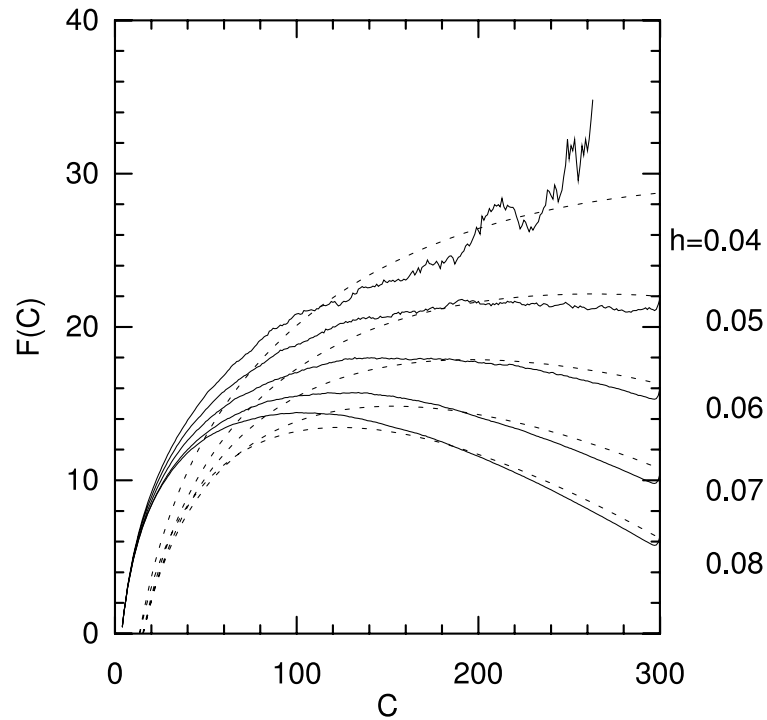


Figure 4.2: Free energy  $F(C)$  as a function of cluster size. The strength of the external field ranges from  $h = 0.04$  (top curve) to  $h = 0.08$  (bottom curve). All measurements are performed at a fixed temperature given by  $\beta J = 0.54$ . The dotted lines are theoretical predictions as given in eq. (4.12), in which the surface tension is given by eq. (4.14). These equations contain no free parameters. However, the free energy offset  $F_0$  which in principle is fixed by normalization of the probability distribution  $p(C)$ , is now adjusted, since otherwise a large vertical shift would result from the inaccuracy of the free energy of small clusters.

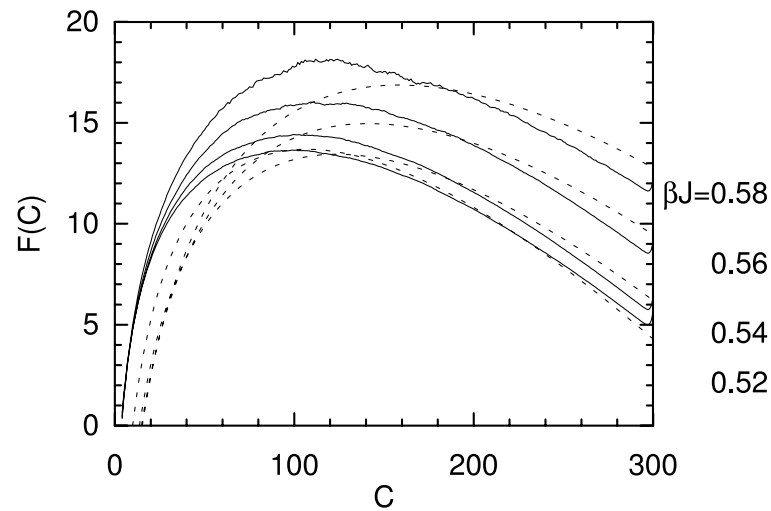


Figure 4.3: Free energy  $F(C)$  as a function of cluster size  $C$ . The temperature ranges from  $\beta J = 0.52$  (bottom curve) to  $\beta J = 0.58$  (top curve). All measurements are performed at a fixed strength of the external field given by  $h = 0.08$ . The dotted lines are theoretical predictions as given in eq. (4.12), in which the surface tension is given by eq. (4.14). These equations contain no free parameters. However, as in the previous figure, the free energy offset  $F_0$  is adjusted.

## 4.4 Simulation results for the rate of growth and shrinkage

Next, we turn to the non-equilibrium results. Figure 4.4 shows the resulting values for the diffusion coefficient  $D_i$ . In CNT, it is commonly assumed that the rate of growth and shrinkage for non-conserved dynamics is simply proportional to the interface area, which scales as  $\sqrt{C}$ . In earlier work, we determined the proportionality constant  $g(\beta J)$  from measurements on the diffusion of a straight interface, in an Ising model on a rectangular lattice with anti-periodic boundary conditions, and showed that it is temperature dependent. The relation between the parameter  $\Gamma_{i,i\pm 1}$  in chapter 3 and the diffusion coefficient  $D_i$  is given by

$$D_i = \Gamma_{i,i+1} + \Gamma_{i,i-1} \approx 2\Gamma_{i,i\pm 1}. \quad (4.15)$$

Figure 4.4 shows the measurements for  $D_i$ , for various  $\beta J$ , at a constant value  $h = 0.08$ , as well as the theoretical prediction  $D_i = g(\beta J)\sqrt{C}$ . We also did measurements at other values of the external field, but these showed that the dependence of  $D_i$  on  $h$  is very small over a wide range of values of  $h$ . The excellent agreement between the measured  $D_i$  and the estimate  $g(\beta J)\sqrt{C}$ , in which  $g(\beta J)$  is obtained from the diffusion of a straight interface in the absence of a driving field, indicates that there is neither a significant dependence on the field strength in the rates of growth and shrinkage of islands, nor on the cluster size, apart from the factor of  $\sqrt{C}$ .

## 4.5 Summary and conclusions

The growth and shrinkage of islands during nucleation in the two-dimensional Ising model has been studied, and compared to the solutions of a Fokker-Planck equation with island-size-dependent drift and diffusion coefficients. We observed that:

- the free energy  $F(C)$  as a function of island size  $C$  is described accurately by the Becker-Döring description Eq. (4.12), for large enough  $C$ , provided that finite-size corrections to the surface tension associated with the closure of the interface are included;
- there is no indication of a significant dependence of the surface tension on strength of the external field;

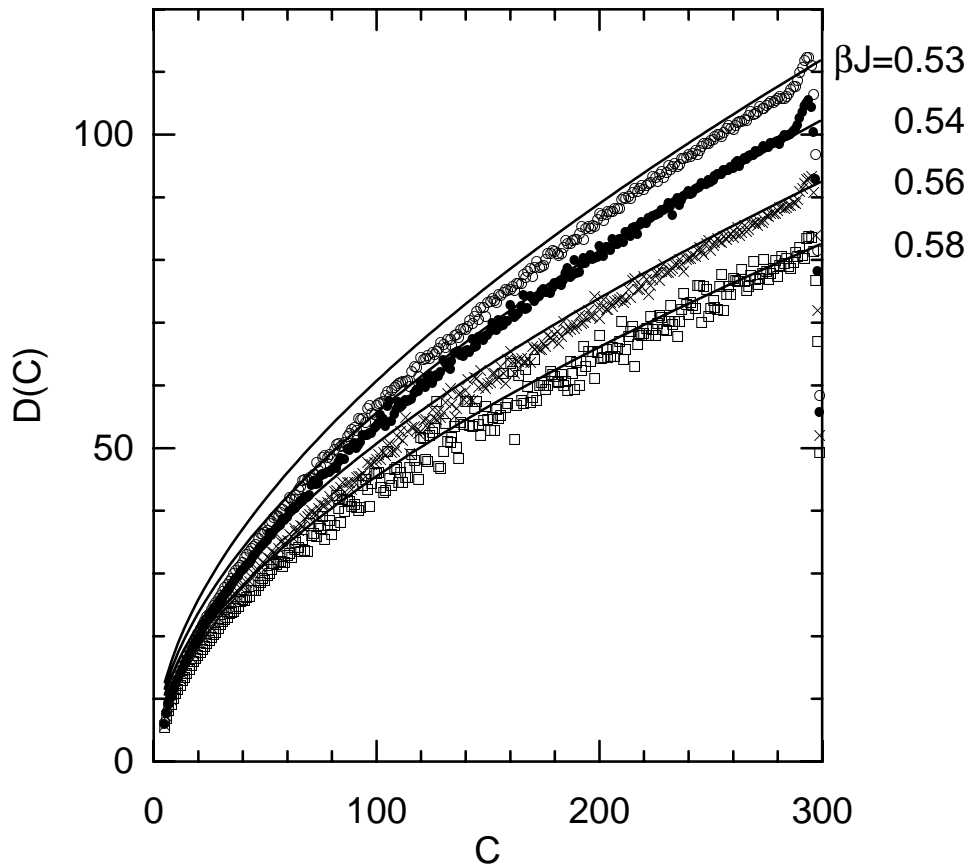


Figure 4.4: Diffusion coefficient  $D_i$  as a function of mass of the nucleating droplet, as obtained from fitting the Fokker-Planck equation to the simulation data.

- the diffusive component  $D_i$  of the rates of growth and shrinkage of islands is in good approximation proportional to  $\sqrt{C}$ , with a temperature-dependent proportionality constant which can be obtained accurately from simulations of interface diffusion;
- there are no indications that this proportionality constant changes with the strength of the external field.

## Appendix: Effective line tension on a cylinder

We consider a membrane on a rectangular lattice with periodicity  $L$  in the shortest direction, which we take to be the  $y$ -direction, and periodicity  $L'$  in the (long)  $x$ -direction. The interface runs parallel to the short direction. Excluding overhangs, one may specify the position of the interface by  $x(y)$ . The energy of an interface configuration is assumed to be proportional to the interface length, with as proportionality constant the bare surface tension:

$$E(x(y)) = \sigma_b \int_0^L \sqrt{1 + \left(\frac{\partial x}{\partial y}\right)^2} dy. \quad (4.16)$$

To enforce a minimal wave length of unity, we discretize the membrane positions:  $y = 1 \dots L$ . We do not discretize the  $x$ -coordinates. Our first goal is to find the eigenmodes of the membrane. It turns out that the appropriate functions are

$$\begin{aligned} f_k(y) &= \frac{1}{\sqrt{2\pi L}} \cos\left(\frac{2\pi ky}{L}\right), k = 0 \dots L/2 \\ g_k(y) &= \frac{1}{\sqrt{2\pi L}} \sin\left(\frac{2\pi ky}{L}\right), k = 1 \dots L/2 - 1 \end{aligned} \quad (4.17)$$

Note that the membrane has  $L$  degrees of freedom, and thus also  $L$  eigenmodes. We can specify the interface configuration as

$$x(y) = \sum_{k=0}^{L/2} a_k f_k(y) + \sum_{k=1}^{L/2-1} b_k g_k(y). \quad (4.18)$$

The transformation is phase-space conserving, *i.e.*, the jacobian of transformation is unity. The modes  $f_k$  and  $g_k$ , excited with amplitudes  $a_k$  and  $b_k$ , are eigenmodes of the membrane:  $\partial^2 E / \partial a_i \partial a_j = 0$  if  $i \neq j$ , and  $\partial^2 E / \partial a_i \partial b_j = 0$ .

The total energy to quadratic order in  $dx/dy$  is thus given by

$$E(C) = E_0 + \frac{\pi\sigma_b}{L^2} \sum_k (a_k^2 + b_k^2)k^2, \quad (4.19)$$

in which  $E_0 = L\sigma_b$  is the ground state energy. The partition function is the integration of the Boltzmann weight  $w_b(C) = \exp(-\beta E(C))$  over all interface configurations  $C$ . To obtain it, we first separate out the sideways displacement of the interface, corresponding to  $a_0$ . This yields a factor of  $L'\sqrt{2\pi L}$  to the partition function. We then integrate over all deformations of the interface:

$$\begin{aligned} Z &= L'\sqrt{2\pi L} \prod_k \int da_k \int db_k \exp(-\beta E(k, a_k, b_k)) \\ &= L'\sqrt{2\pi L} \exp(-\beta E_0) \cdot \prod_k \int da_k \int db_k \exp\left[-\beta\sigma_b \frac{(a_k^2 + b_k^2)k^2}{L^2}\right] \\ &= L'\sqrt{2\pi L} \exp(-\beta E_0) \cdot \left(\prod_k \sqrt{\frac{\beta\sigma_b k}{\pi L}}\right)^{-2} \\ \Leftrightarrow \log(Z) &= \log(L') + \frac{1}{2} \log(2\pi L) - \beta E_0 - 2 \sum_{k=1}^{L/2-1} \log\left(\sqrt{\frac{2\beta\sigma_b k}{\pi L/2}}\right) \\ &= \log(L') + \frac{1}{2} \log(2\pi L) - \beta E_0 - (L-2) \log\left(\frac{2\beta\sigma_b}{\pi}\right) - 2 \sum_{k=1}^{L/2-1} \log\left(\frac{k}{L/2}\right) \\ &= \log(L') - \frac{1}{2} \log(2\pi L) - \beta E_0 - (L-2) \log\left(\frac{2\beta\sigma_b}{\pi}\right) + L \quad (4.20) \end{aligned}$$

We then obtain

$$\begin{aligned} \beta F &\equiv \log(L') - \log(Z) \\ &= \beta\sigma_b L + \frac{1}{2} \log(2\pi L) + (L-2) \log\left(\frac{2\beta\sigma_b}{\pi}\right) - L. \quad (4.21) \end{aligned}$$

From this result, we can obtain the interfacial tension as

$$\sigma_{\text{eff}} \equiv \frac{F}{L} + \log(L') \approx \sigma_b - \frac{1}{\beta} + \frac{1}{2\beta} \frac{\log(L)}{L} + \mathcal{O}\left(\frac{1}{L}\right). \quad (4.22)$$

Note that the second term scales inversely proportional to  $\beta$ , and hence is an entropic correction. One can interpret this entropic correction as arising

from the difficulty that the interface has to connect to itself through the periodic direction; alternatively, one can argue that it arises from the cut-off in the capillary oscillations: the periodicity with  $L$  reduces oscillations to multiples of  $k = (2\pi L)^{-1}$ .

The short-wavelength behavior of the energy is not always described properly by Eq. (4.19). For instance in the case of the Ising model, not only the  $x$ -coordinates are discretized, but also the  $y$ -coordinates, and the energy becomes

$$E = \sigma_b \sum_k \frac{a_k^2 + b_k^2}{2\pi} [1 - \cos(2\pi k/L)]. \quad (4.23)$$

Again, we integrate over all deformations of the interface:

$$\begin{aligned} Z &= L' \sqrt{2\pi L} \prod_k \int da_k \int db_k \exp(-\beta E(k, a_k, b_k)) \\ &= L' \sqrt{2\pi L} \exp(-2\beta L) \cdot \prod_k \int da_k \int db_k \exp[-\beta \frac{a_k^2 + b_k^2}{2\pi} [1 - \cos(2\pi k/L)]] \\ &= L' \sqrt{2\pi L} \exp(-2\beta L) \cdot \left( \prod_k \sqrt{\frac{\beta}{2} (1 - \cos(2\pi k/L))} \right)^{-2}, \end{aligned} \quad (4.24)$$

which gives

$$\begin{aligned} \log(Z) &= \log(L') + \frac{1}{2} \log(2\pi L) - 2\beta L - \sum_{k=1}^{L/2-1} \log \left( 1 - \cos \left( \frac{2\pi k}{L} \right) \right) \\ &\quad - \left( \frac{L}{2} - 1 \right) \log \left( \frac{\beta}{2} \right) \\ &= \log(L') + \frac{1}{2} \log(2\pi) - \frac{1}{2} \log(L) - 2\beta L \\ &\quad - \left( \frac{L}{2} - 1 \right) \log \left( \frac{\beta}{2} \right) + \frac{1}{2} \log(2)L. \end{aligned} \quad (4.25)$$

In the last step, we used

$$\sum_{k=1}^{L/2-1} \log(1 - \cos(2\pi k/L)) = -\frac{1}{2} \log(2) L + \log(L). \quad (4.26)$$

This yields the same logarithmic correction to the surface tension. Apparently, the logarithmic correction, including its prefactor, is not sensitive to the exact behavior of the energy at short wavelengths.

In the case of the two-dimensional Ising model, finite-size effects to the surface tension can be obtained exactly, using a system with periodic boundary conditions in one direction and antiperiodic boundary conditions in the other direction. McCoy and Wu [9], in Eq.(4.31) of chapter V, report the ratio of the partition sums  $Z_p$  and  $Z_a$  for the Ising model on an  $L \times M$  lattice with periodic and anti-periodic boundary conditions, respectively, for large enough  $L$ , as

$$Z_p/Z_a = \frac{1}{2M} a(\pi)^{-L} \sum_{k=0}^{\infty} \exp\left(-\frac{1}{2} \frac{a''(\pi)}{a(\pi)} \frac{\pi^2 k^2 L}{M^2}\right). \quad (4.27)$$

where  $a(\pi)$  and  $a''(\pi)$  are constants. This gives, after approximating the sum by an integral

$$Z_p/Z_a = a(\pi)^{-L} \sqrt{\frac{a(\pi)}{8\pi a''(\pi)L}}. \quad (4.28)$$

This yields for the surface tension

$$\sigma_{\text{eff}} = \log(Z_p/Z_a)/(\beta L) = \sigma_{\infty} + \frac{1}{2\beta} \frac{\log(L)}{L}. \quad (4.29)$$

Also this approach to estimate the entropic finite-size effects to the interfacial tension yields the same logarithmic correction.

The method used above can also be used to approximate the finite size corrections to the surface tension of a droplet. We consider a (roughly circular) droplet with radius  $R$ , area  $A = \pi R^2$  and perimeter  $L \approx 2\pi R$ , located on an  $L' \times L'$  lattice with periodic boundary conditions. Considering initially the situation where the center of mass of the droplet is not too far from the origin, we specify the shape of the island in polar coordinates, by the distance  $r(\phi)$  from the origin to the perimeter, along a direction with angle  $\phi$  with respect to the  $x$ -axis.

The first step is again to find a phase-space conserving transformation to a basis that diagonalizes the hessian. Moreover, we demand that the first degree of freedom corresponds to radial expansion/contraction, and the second and third degree of freedom to horizontal and vertical translation.

The transformation in polar coordinates specified by

$$r(\phi) = R + \Delta \cos(\phi) - \frac{\Delta^2}{4R} (1 - \cos(2\phi)) + \mathcal{O}(\Delta^4) \quad (4.30)$$

can be shown to correspond to a translation: written in Cartesian coordinates  $x = r \cos(\phi)$  and  $y = r \sin(\phi)$ , one obtains

$$(x - \Delta)^2 + y^2 - R^2 = \frac{\Delta^4}{4R^2} \sin^4(\phi) = \mathcal{O}(\Delta^4). \quad (4.31)$$

A basis as we are after is then obtained with the functions

$$\begin{aligned} f_k(\phi) &= \frac{\cos(k\phi)}{\sqrt{2\pi L}}; k = 0 \dots L/2 \\ g_k(\phi) &= \frac{\sin(k\phi)}{\sqrt{2\pi L}}; k = 1 \dots L/2 - 1. \end{aligned} \quad (4.32)$$

This yields  $L$  degrees of freedom, as many as there were with a straight interface of the same length in Appendix 1. A slight problem is that excitations of modes  $f_k(\phi)$  or  $g_k(\phi)$  do not preserve the area of the droplet. We can however correct this with correction terms of order  $a_k^2$  and  $b_k^2$ , and write

$$\begin{aligned} r(\phi) &= R + a_0 + \sum_{k=1}^{L/2} a_k f_k(\phi) + \sum_{k=1}^{L/2-1} b_k g_k(\phi) - \frac{1}{4L^2} \sum_{k=1}^{L/2-1} (a_k^2 + b_k^2) \\ &= R' + a_0 + \sum_{k=1}^{L/2} a_k f_k(\phi) + \sum_{k=1}^{L/2-1} b_k g_k(\phi), \end{aligned} \quad (4.33)$$

in which  $R' = R - \frac{1}{4L^2} \sum_{k=1}^{L/2-1} (a_k^2 + b_k^2)$ . In this expression, the term  $a_0$  is the amplitude for the  $k = 0$  mode of radial expansion/contraction,  $a_1$  and  $b_1$  are the amplitudes for the  $k = 1$  modes of horizontal and vertical translation, and the last term is required to preserve the droplet area for excitations in the modes with nonzero  $k$ ; it is easy to verify that the droplet area  $\frac{1}{2} \int d\phi r^2(\phi)$ , is preserved.

In the continuum limit, the energy of the interface scales linearly with the contour length of the interface:

$$E = 2J \int d\phi \sqrt{r(\phi)^2 + \left(\frac{dr}{d\phi}\right)^2}. \quad (4.34)$$

As before, the modes  $f_k(\phi)$  and  $g_k(\phi)$  are eigenmodes of the hessian; luckily, the higher-order terms that keep the area conserved do not alter

this. We then obtain for the total energy

$$\begin{aligned} E &= 4\pi J R' + \pi J \sum_{k=1}^{L/2-1} \frac{k^2(a_k^2 + b_k^2)}{L^2} \\ &= 2LJ + \pi J \sum_{k=1}^{L/2-1} \frac{(a_k^2 + b_k^2)(k^2 - 1)}{L^2}. \end{aligned} \quad (4.35)$$

Taking into consideration the discreteness of the coordinate  $y = \phi R$  along the perimeter, the energy associated with a small excitation of the mode  $f_k(\phi)$  with amplitude  $a_k$  equals

$$E = 2J \sum_{y=0}^{L-1} \sqrt{\left(\frac{R'}{R}\right)^2 + \frac{a_k^2}{2\pi L} \left[ \cos\left(\frac{k(y+1)}{R}\right) - \cos\left(\frac{ky}{R}\right) \right]^2}. \quad (4.36)$$

Assuming small excitations  $a_k$ , this can be rewritten as

$$E = 4\pi J R' + J \int_0^L \frac{a_k^2}{2\pi L} \left[ \cos\left(\frac{k(y+1)}{R}\right) - \cos\left(\frac{ky}{R}\right) \right]^2 dy, \quad (4.37)$$

or equivalently,

$$E - E_0 = J \frac{a_k^2}{2\pi} [1 - \cos(2\pi k/L)] - \frac{\pi J a_k^2}{L^2}. \quad (4.38)$$

The same expression holds for excitations of  $g_k(y)$  with amplitude  $b_k$ .

The difference between the energy of the straight and circular interfaces with the same length, apart from the  $k = 0$  and  $k = 1$  modes, lies in the replacement of  $k^2$  by  $k^2 - 1$ . Regarding these modes with  $k > 1$ , we obtain

$$\begin{aligned} \log(Z_c) - \log(Z_l) &= \sum_{k=2}^{L/2-1} \log(k^2/L^2) - \sum_{k=2}^{L/2-1} \log((k^2 - 1)/L^2) \\ &= \sum_{k=2}^{L/2-1} \log(k^2/(k^2 - 1)) = \mathcal{O}(L^{-1}) \end{aligned} \quad (4.39)$$

The contribution of the mode with  $k = 1$  to the cylinder is  $\log(1/L^2) = -2\log(L)$ , while the  $k = 0$  mode contributes  $\log(L') + \frac{1}{2}\log(L)$ . For the circular interface on an  $L' \times L'$  system, there are two  $k = 1$  (translational)

modes, each contributing  $\log(L') + \frac{1}{2} \log(L)$ , and the  $k = 0$  mode contributes  $\frac{1}{2} \log(L)$ .

Recalling that the interface on a cylinder had a free energy of  $\beta F = aL + \frac{1}{2} \log(L)$ , we thus obtain for a circular island:

$$\beta F = aL + \frac{3}{2} \log(L) + \mathcal{O}(1), \quad (4.40)$$

or

$$\sigma \approx \sigma_{L=\infty}(\beta) + \frac{3}{2\beta} \frac{\log(L)}{L} + \mathcal{O}(L^{-1}). \quad (4.41)$$

## Chapter 5

# Fluctuations of the geomagnetic dipole

### 5.1 Introduction

The strength of the Earth's virtual axial dipole moment (VADM) shows a considerable time variability, about 25% rms of the mean, over the course of thousands of years.[32] Occasionally, the variations are so large that the sign of the dipole moment changes. These reversals happen roughly once per  $(2 - 3) \times 10^5$  yr.[33] Apart from its sign, the correlation time of the VADM is only a few thousand years. The geomagnetic field is the result of inductive processes in the Earth's liquid metallic outer core. Helical convection amplifies the magnetic field and balances resistive decay. Several groups have confirmed this idea with the help of numerical simulations[34, 35, 36].

Since the VADM is the result of many processes taking place in the convecting metallic outer core that interact with each other in a complicated way, it makes sense to try and describe the time evolution of the VADM over time scales of thousands of years as a stochastic process. Based on the equations of Magnetohydrodynamics (MHD), Hoyng et al.[37] proposed that the dynamics of the VADM can be described by a set of coupled differential equations, which include a term with multiplicative noise. In this model, the multipole components of the geomagnetic field behave as a multidimensional bistable oscillator driven by multiplicative noise. In a follow-up study Hoyng et al.[38] were able to reproduce the main observed facts: fast and large fluctuations around a mean VADM and occasional reversals with time scales of the right magnitude. Hoyng and Duistermaat

(HD)[39] considered a simplified version of that model and succeeded to compute the mean time between reversals from first principles.

One of the simplest equations that can be used to describe stochastic dynamics is the Fokker-Planck equation:[40]

$$\frac{\partial \rho(x, t)}{\partial t} = -\frac{\partial}{\partial x}(v\rho) + \frac{1}{2} \frac{\partial^2}{\partial x^2} (D\rho) . \quad (5.1)$$

Here,  $t$  is time,  $x$  the strength of the VADM, and  $\rho(x, t)$  is the probability density for  $x$  and time  $t$ , while  $v(x)$  and  $D(x)$  are the  $x$ -dependent average "velocity" (that is,  $v = \langle dx/dt \rangle$ ) and diffusion coefficient, respectively. Such an equation for the probability density of the dipole amplitude has actually been derived in ref. [37].

Here we follow a somewhat different approach. We start from the VADM observations and study these as a realization of a stochastic process. Specifically, we investigate whether the time evolution of the VADM can be described by a Fokker-Planck equation (5.1) with suitably chosen velocity and diffusion coefficient, and if so, how the velocity and diffusion coefficient depend on the magnitude  $x$  of the VADM. We perform this procedure both on the output of the HD model and on the data known under the name Sint-800,[32] and we discuss our findings.

## 5.2 Method

We start with the discretized version of the Fokker-Planck equation. Discretization of space and time in Eq. 5.1 leads to

$$\begin{aligned} \frac{\rho_i(t + \Delta t) - \rho_i(t)}{\Delta t} = & -\frac{v_{i+1}\rho_{i+1}(t) - v_{i-1}\rho_{i-1}(t)}{2\Delta x} \\ & + \frac{D_{i+1}\rho_{i+1}(t) + D_{i-1}\rho_{i-1}(t) - 2D_i\rho_i(t)}{2(\Delta x)^2} . \end{aligned} \quad (5.2)$$

We may rewrite this equation in matrix form as

$$\rho_i(t + \Delta t) = \sum_j (\delta_{ij} + \Delta t M_{ij}) \rho_j(t) , \quad (5.3)$$

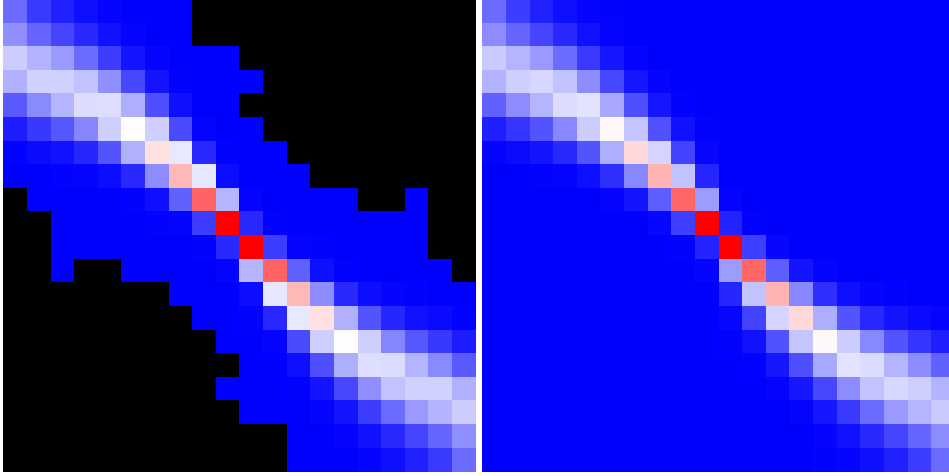


Figure 5.1: Left: the transition matrix  $T$  as obtained from simulation data of the HD model. Right: the approximate transition matrix  $\tilde{T}$ , obtained from a tridiagonal matrix  $M$  raised to the power  $\tau/\Delta t$ . The upper left corner corresponds to  $(-2, -2)$ , the lower right to  $(2, 2)$ . The bin size is  $0.2 \times 0.2$ . The matrix elements obey  $0 \leq T_{i,j} < 1$ . The colour scale runs from black ( $= 0$ ), then gradually from blue to white ( $= 0.5$ ), then from white to red ( $= 1$ ).

where  $M$  is a tridiagonal matrix with elements

$$\begin{aligned}
 M_{i,i-1} &= \frac{v_{i-1}}{2\Delta x} + \frac{D_{i-1}}{2(\Delta x)^2} ; \\
 M_{i,i} &= -\frac{D_i}{(\Delta x)^2} ; \\
 M_{i,i+1} &= -\frac{v_{i+1}}{2\Delta x} + \frac{D_{i+1}}{2(\Delta x)^2} .
 \end{aligned} \tag{5.4}$$

By solving for  $v_i$  and  $D_i$  we obtain

$$\begin{aligned}
 v_i &= (M_{i+1,i} - M_{i-1,i}) \Delta x ; \\
 D_i &= (M_{i+1,i} + M_{i-1,i}) (\Delta x)^2 .
 \end{aligned} \tag{5.5}$$

These expressions will be used to infer  $v_i$  and  $D_i$  once the matrix  $M$  has been determined.

Each column of  $M$  adds up to zero,  $M_{i-1,i} + M_{i,i} + M_{i+1,i} = 0$ , so that there are two free parameters per spatial interval  $i$ , exactly as many as

the parameters  $v_i$  and  $D_i$  in the Fokker-Planck equation. An important consequence of the zero column sum is that eq. (5.3) is norm-conserving,

$$\sum_i \rho_i(t + \Delta t) = \sum_i \rho_i(t) . \quad (5.6)$$

Note, finally, that in the limit  $\Delta t \rightarrow 0$  eq. (5.3) becomes

$$\frac{d\rho_i}{dt} = \sum_j M_{ij} \rho_j . \quad (5.7)$$

The object of our work is to extract the effective position-dependent velocity and diffusion coefficient from a time series, in this case of the strength of the Earth's magnetic dipole moment. To this end we construct from the data the matrix  $T$  whose elements  $T_{i,j}$  contain the frequencies with which a system that is located in position  $j$  at some time  $t$ , will be in position  $i$  at time  $t + \tau$ . Here  $\tau$  is chosen comparable to, or larger than the VADM autocorrelation time, so that the system can be described as a Markov chain.

By construction,  $T_{i,j}$  specifies how a probability density that is initially concentrated at position  $j$  is redistributed over positions  $i$  after a time  $\tau$ . The stationary distribution  $p_i$  is invariant for such a redistribution, so  $p_i$  must be an eigenvector of  $T$  with eigenvalue 1. The other eigenvalues of  $T$  all have a magnitude smaller than 1 because of positivity of probability at all times. We then determine  $p_i$  as the leading eigenvector of  $T$ . Since  $p_i$  is the probability that the system finds itself in state  $i$ , we may also determine  $p_i$  simply by binning of the data, and the two results do not differ significantly.

Our assumption is that the process can be described effectively by eq. (5.3) for sufficiently small  $\Delta t$ . The corresponding prediction for transitions from position  $i$  to  $j$  over a time difference of  $\tau \gg \Delta t$  is then

$$\tilde{T} = (I + \Delta t M)^{\tau/\Delta t} . \quad (5.8)$$

The task at hand is to find  $M$  by an appropriate comparison of  $(I + \Delta t M)^{\tau/\Delta t}$  with  $T$ . If the number of spatial intervals is equal to  $n$ , the matrix  $M$  has approximately  $3n$  elements (ignoring end effects), of which roughly  $n$  may be eliminated by imposing norm conservation (columns add up to zero), and another  $n$  by using  $\sum_j M_{ij} p_j = 0$ . This last property follows because the stationary distribution should obey eq. (5.7).

A naive approach would be to transform the matrix  $T$  to the basis of its eigenvectors, raise all eigenvalues to the power  $\Delta t/\tau$ , and to transform

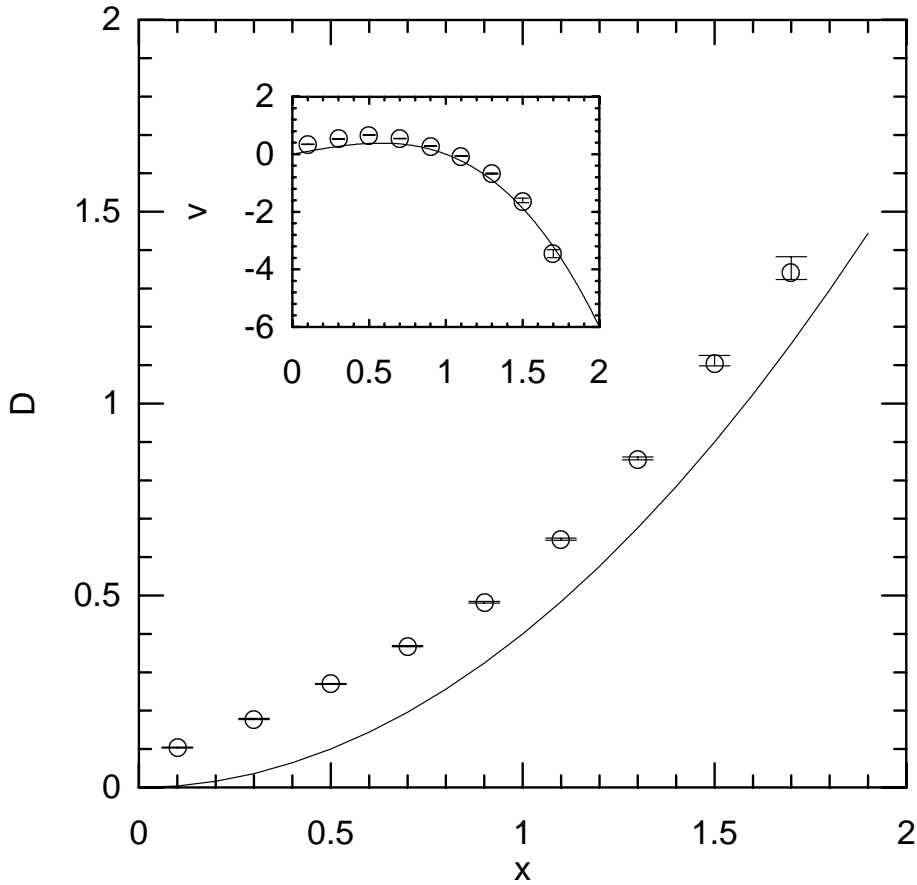


Figure 5.2: The diffusion coefficient  $D$  as a function of  $x$  (dimensionless VADM), as obtained from fitting the simulation data of ref. [39] to the Fokker-Planck equation. The drawn line is  $D_0 x^2$  from eq. (5.10). The inset shows the velocity  $v(x)$ , compared to the theoretical value  $x(1-x^2)$  (drawn line). See text for details.

back to the original basis. In practice, this does not work. The eigenvectors of  $T$  with small eigenvalues correspond to quickly decaying states and are therefore very noisy. However, even small eigenvalues become significant once they are raised to a small power  $\Delta t/\tau \sim 1/100$ , and they contribute significantly to  $M$ . Therefore, we follow a different approach to find the remaining  $n$  degrees of freedom in  $M$ : we perform a minimization of  $\|T - (I + \Delta t M)^{\tau/\Delta t}\|$ . This minimization is implemented using the routine E04FCF of the NAG library.

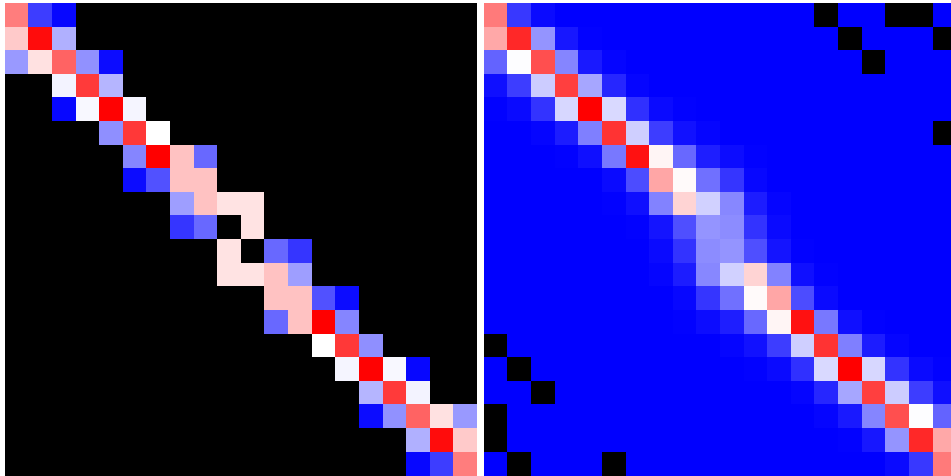


Figure 5.3: Left: the transition matrix  $T$  obtained from the Sint-800 data. Right: the approximate transition matrix  $\tilde{T}$  obtained from a tridiagonal matrix  $M$  raised to the power  $\tau/\Delta t$ . The upper left corner corresponds to  $(-10, -10) \cdot 10^{22} \text{Am}^2$ , and the lower right corner to  $(10, 10) \cdot 10^{22} \text{Am}^2$ . We use square bins of linear size  $1 \cdot 10^{22} \text{Am}^2$ . The colour coding is the same as in Fig. 5.1.

### 5.3 Results on the HD model

First, we test the approach outlined above on data generated with the HD model, see Fig. 2 of ref. [39]. This is a time series  $x(t)$  of VADMs measured in units of its equilibrium value, extending over 5000 time units. This corresponds approximately to 50-100 My, as time is measured in terms of the linear growth time of the dipole mode. We discretize the strength of the VADM  $x(t)$  into 20 bins of width 0.2 in dimensionless units. Next, we make a histogram of all sets  $\{x(t), x(t + \tau)\}$  with  $\tau = 0.16$  (in HD units), which yields  $T$ . We exploit the fact that there is no sign preference, that is, for a given realization  $x(t)$  the series  $-x(t)$  is an equally likely realization. Accordingly, we add to the histogram all sets  $\{-x(t), -x(t + \tau)\}$ . The resulting effective transition matrix  $T$  is plotted in Fig. 5.1 (left). We then perform the fitting procedure outlined above, to obtain the tridiagonal transition matrix  $M$ , with  $\Delta t = \tau/100$ . In the right panel of Fig. 5.1, we have also plotted  $\tilde{T}$  obtained from  $M$  according to eq. (5.8). There is a clear similarity between the two matrices.

Figure 5.2 shows the resulting values for the diffusion coefficient  $D_i$

and the velocity  $v_i$  (inset). To place these in perspective, we compute the Fokker-Planck equation for the probability density of  $x$  by integrating eq. (5) and (6) of ref. [39] over the overtone amplitude  $r$ , to find

$$\frac{\partial \rho}{\partial t} = -\frac{\partial}{\partial x} x(1-x^2)\rho + \frac{1}{2} \frac{\partial^2}{\partial x^2} D_0(x^2 + \langle r^2 \rangle)\rho . \quad (5.9)$$

In other words, we recover eq. (5.1) with

$$v = x(1-x^2) ; \quad D = D_0(x^2 + \langle r^2 \rangle) . \quad (5.10)$$

Here  $\langle r^2 \rangle$  is the (unknown) mean square overtone amplitude for given  $x$ , and  $D_0$  a constant equal to 0.4 for the dataset used here.

The  $v$  and  $D$  recovered from the data compare rather well with their theoretical values (5.10). Unfortunately, we cannot make a more detailed comparison, as it is not possible to compute the  $x$ -dependence of  $\langle r^2 \rangle$ . But the value of  $\langle r^2 \rangle$  from the simulations agrees with the value implied by Fig. 5.2. We conclude that the approximate description of the complicated HD model by a Fokker-Planck equation works rather well.

## 5.4 Results on Sint-800 data

We then repeat this procedure on the Sint-800 data [32]. This is a series of 800 VADM measurements covering the past 800 ky. We changed the sign of the VADM for  $t > 780$  ky to allow for the fact that a reversal took place then. [41] The fitting procedure was performed with a time lag of  $\tau = 2$  ky and a fitting time step of  $\Delta t = \tau/100$ , see Fig. 5.3. The resulting velocity  $v_i$  and diffusion coefficient  $D_i$  are shown in Fig. 5.4. The error bars in Fig. 5.4 are 20-80% confidence intervals constructed as follows. Before normalization, each matrix element  $T_{i,j}$  is a natural number, and we assign to it a standard deviation equal to the square root of the number  $T_{i,j}$ . Next we normalize and draw from a normal distribution to obtain new values of  $T_{i,j}$ . In this way we construct 20 realizations of the matrix  $T$ , and we repeat the analysis for each of these. In reality, the errors will be larger as we did not account for the intrinsic errors in the VADM data, which are of the order of 10%. [32]

The  $x$  dependence of  $v_i$  is approximately as expected. The best fit of the function  $\lambda x[1 - (x/x_0)^2]$  used in the HD model to the data  $v_i$  yields  $1/\lambda = 20_{-10}^{+20}$  ky, and  $x_0 = 6.4$  Am<sup>2</sup>. The  $x$ -dependence of the diffusion coefficient  $D_i$  is quite different from what one would expect, as there is no sign of multiplicative noise. These results are discussed below.

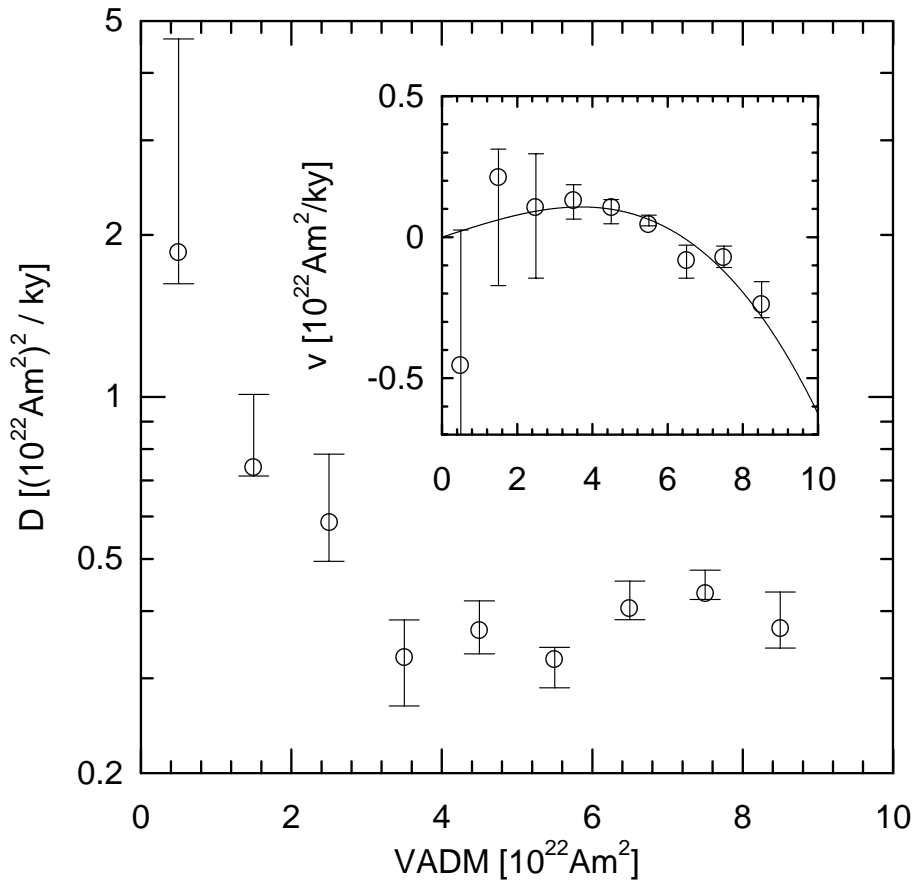


Figure 5.4: Diffusion coefficient  $D_i$  and velocity  $v_i$  (inset) as a function of magnetic dipole strength, obtained from fitting the Fokker-Planck equation to the Sint-800 data. The drawn line in the inset is the best fit of  $\lambda x[1 - (x/x_0)^2]$  to the  $v_i$ , see text for details.

## 5.5 Conclusions and discussion

To begin with the HD model, our results demonstrate that our analysis of the time series is capable to extract the information on the systematic flow  $v_i$  and the type of noise that was used in the model. The scaling  $D \propto x^2$  is a consequence of the multiplicative noise that the HD model employs (that is, a noise term of the type  $\dot{x} = \dots + N(t)x$ ). As explained in ref. [39], this type of noise is inherent in the induction equation of MHD with a

fluctuating velocity term:  $\partial \mathbf{B} / \partial t = \nabla \times \mathbf{v}_0 \times \mathbf{B} + \nabla \times \delta \mathbf{v} \times \mathbf{B} + \eta \nabla^2 \mathbf{B}$ . The fluctuating velocity  $\delta \mathbf{v}$  acts multiplicatively on  $\mathbf{B}$ . It represents the convective turbulence in the metallic iron core, superposed on a steady flow  $\mathbf{v}_0$ .

The fact that  $D \neq 0$  for  $x = 0$  is due to the overtone in the HD model and is responsible for the occurrence of reversals. For small  $x$  we have  $v \propto x$  which corresponds to linear growth of the dipole mode when it is small, and the  $-x^3$  term is the nonlinear quenching used in the HD model. More important than these physical details is the fact that we have validated the method: our analysis is able to get out what has been put into the model.

The analysis of the Sint-800 data confirms that the geomagnetic dipole mode is unstable with a linear growth time  $1/\lambda \simeq 20_{-10}^{+20}$  ky. Note that the nonlinear quenching is well described by the quadratic quenching function  $[1 - (x/x_0)^2]$ . The nonlinear equilibrium is attained at a VADM of  $x_0 = 6.4 \cdot 10^{22} \text{ Am}^2$ . These results are more or less as expected, but to our knowledge this is the first time that  $\lambda$  and the shape of the quenching function have been estimated for VADM data.

Our results on the diffusion coefficient are enigmatic. The increase of the diffusion coefficient for  $|x| \rightarrow 0$  is probably an artifact of the restricted length of the data set, in combination with the fact that only one reversal occurred in the last 800 ky, while the average frequency of reversals is once per 200 to 300 ky. VADMs smaller than  $2 \times 10^{22} \text{ Am}^2$  are absent in the Sint-800 data except during the one (very brief) reversal period. For  $\text{VADM} > 3 \times 10^{22} \text{ Am}^2$  the diffusion coefficient is constant. There is no sign of multiplicative noise in the Sint-800 data, and we believe that this is a solid result. The data seem to indicate that the noise is quasi-additive. We have no explanation for this, but one possibility is that it is due to a nonlinear quenching of the velocity fluctuations  $\delta \mathbf{v}(t)$ . Another possibility is related to the amplitude of the overtone fluctuations. The HD model has only one overtone (for simplicity) but the geodynamo has of course many. Their combined effect might result in a diffusion coefficient with unexpected dependence on the dipole strength  $x$ .

We regard this study as a first step in the analysis of time series of geomagnetic data. One way to improve our conclusions on the geodynamo would be to use a longer dataset. At the time of writing, no longer VADM time series of the geodynamo were available to us. But an interesting alternative is to use VADM data from hydromagnetic simulations.



# Bibliography

- [1] K. Brendel, G. T. Barkema and H. van Beijeren, Phys. Rev. E **67**, 026119 (2003).
- [2] K. Brendel, G. T. Barkema and H. van Beijeren, Phys. Rev. E **71**, 031601 (2005).
- [3] P. A. Rikvold, G. Brown, S. J. Mitchell and M. A. Novotny, *Dynamics of Magnetization Reversal in Models of Magnetic Nanoparticles and Ultrathin Films* Submitted to Springer Lecture Notes in Physics, cond-mat/0110103.
- [4] A. Misra and B. K. Chakrabarti, Europhys. Lett. **52**, 311 (2000).
- [5] M. P. Nightingale and H. W. J. Blöte, Phys. Rev. B **62**, 1089 (2000).
- [6] P. Hänggi, P. Talkner and M. Borkovec, Rev. Mod. Phys. **62**, 251 (1990).
- [7] A. M. Ferrenberg and R. H. Swendsen, Phys. Rev. Lett. **63**, 1195 (1989).
- [8] S. Auer and D. Frenkel, Nature **409**, 1020 (2001).
- [9] B. M. McCoy and T. T. Wu, "The two-dimensional Ising model", Harvard University Press, Cambridge, Mass., 1973.
- [10] N. Metropolis, A. W. Rosenbluth, M. N. Rosenbluth, A. H. Teller, and E. Teller, J. Chem. Phys. **21**, 1087 (1953).
- [11] McCoy and Wu give the partition function for a system with non-helical boundary conditions, whereas we have used helical boundary conditions. This should only make a difference at very low temperatures.

- 
- [12] P. G. Debenedetti, “*Metastable Liquids*”, (Princeton University Press, Princeton, 1996).
- [13] P. A. Rikvold and B. M. Gorman, Annual Reviews of Computational Physics I, edited by D. Stauffer (World Scientific, Singapore, 1994), pp. 149-191.
- [14] M. Volmer and A. Weber, Z. Phys. Chem. **119**, 277 (1926).
- [15] Z. Farkas, Z. Phys. Chem. A **125**, 236 (1927).
- [16] R. Becker and W. Döring, Ann. Phys. (Leipzig) **24**, 719 (1935).
- [17] J. B. Zeldovich, Acta Physicochim. **18**, 1 (1943).
- [18] P. A. Rikvold, H. Tomita, S. Miyashita and S. W. Sides, Phys. Rev. E **49**, 5080 (1994).
- [19] M. A. Novotny, P. A. Rikvold, M. Kolesik, D. M. Townsley, R. A. Ramos, J. Non-Cryst. Solids **274**, 356 (2000).
- [20] V. A. Shneidman, K. A. Jackson and K. M. Beatty, Phys. Rev. B **59**, 3579 (1999).
- [21] J. L. Harland and W. van Meegen, Phys. Rev. E **55**, 3054 (1997).
- [22] L. Gránásy and T. Pusztai, J. Chem. Phys. **117**, 10121 (2003).
- [23] M. Acharyya and D. Stauffer, European Physical Journal B **5**, 571 (1998).
- [24] V. A. Shneidman, K. A. Jackson and K. M. Beatty, J. Chem. Phys. **111**, 6932 (1999).
- [25] Th. Neuhaus and J. S. Hager, J. Stat. Phys. **113**, 47 (2003).
- [26] A. Coniglio and W. Klein, J. Phys. A **12**, 2775 (1980).
- [27] M. E. J. Newman and G. T. Barkema, “Monte Carlo methods in statistical physics”, Oxford University Press, Oxford, 1999.
- [28] R. C. Tolman, J. Chem. Phys. **17**, 333 (1949).
- [29] L. Onsager, Phys. Rev. **65**, 117 (1944).

- 
- [30] J. E. Avron, H. van Beijeren, L. S. Schulman and R. K. P. Zia, *J. Phys. A* **15**, L81 (1982).
- [31] H. van Beijeren, *J. Stat. Phys.* **110**, 1397 (2003).
- [32] Y. Guyodo and J.-P. Valet, *Nature* **399**, 249-252 (1999).
- [33] Merrill, R.T., McElhinny, M.W. and McFadden, P.L., *The Magnetic Field of the Earth*, Academic Press (1996).
- [34] Glatzmaier, G.A. and Roberts, P.H., *Nature* **377**, 203 (1995).
- [35] Kuang, W. and Bloxham, J., *Nature* **389**, 371 (1997).
- [36] Christensen U., Olson, P. and Glatzmaier, G.A., *Geophys. J. Int.* **138**, 393 (1999).
- [37] Hoyng, P., Ossendrijver, M.A.J.H. and Schmitt, D., *Geophys. Astrophys. Fluid Dynamics* **94**, 263 (2001)
- [38] Hoyng, P., Schmitt, D. and Ossendrijver, M.A.J.H., *Phys. Earth Planet. Int.* **130**, 143 (2002)
- [39] Hoyng, P. and Duistermaat, J.J., *Europhys. Lett.* **68**, 177 (2004). (HD)
- [40] Gardiner C.W., *Handbook of Stochastic Methods*, Springer-Verlag, Berlin (1990).
- [41] Ref. [33], p. 170.



# Samenvatting

Als een gas of vloeistof langzaam afgekoeld wordt zal beneden een bepaalde temperatuur condensatie of bevrozing optreden. Dit betekent dat de moleculen zich ordenen in een druppel of kristalstructuur. Deze processen, waarbij een vaste stof ontstaat uit een vloeistof of een vloeistof uit een gas, zijn voorbeelden van fase-overgangen.

Bij niet al te sterke afkoeling van een systeem zonder onzuiverheden waarin de wand geen speciale rol speelt, zal de overgang naar de stabiele fase plaatsvinden via *homogene nucleatie*: Ergens in het systeem ontstaat door spontane fluctuaties een kern van moleculen in de stabiele fase, die vervolgens groeit totdat het hele systeem zich in deze fase bevindt.

De tijd die het systeem nodig heeft om deze overgang te maken kan heel lang zijn. Dit komt doordat een kern pas de neiging heeft te groeien als hij groter is dan een bepaalde kritische afmeting. Rond de kern bevindt zich een grensvlak tussen bijvoorbeeld de vaste en de vloeibare fase. De vrije energie per oppervlakte-eenheid van dit grensvlak heet de oppervlakte-spanning. De winst in vrije energie ten gevolge van de lagere vrije energie van de stabiele fase is eerst kleiner dan de vrije energie ten gevolge van de oppervlaktetenspanning, maar wint uiteindelijk doordat het volume harder groeit dan de oppervlakte.

In dit proefschrift worden bijdragen gepresenteerd aan de theorie die op grond van materiaaleigenschappen voorspelt hoe lang het duurt voordat nucleatie plaats vindt en wordt deze theorie getest door middel van computersimulaties. Het specifieke "materiaal" is een twee-dimensionaal roostergas, waar theoretisch heel veel van bekend is, omdat het mathematisch equivalent is aan het Isingmodel. Ook is dit model zeer geschikt voor het doen van computersimulaties.

In hoofdstuk 2 wordt gekeken naar het Isingmodel op een lang en smal rooster dat heen en weer springt tussen twee stabiele fasen. De voorspelling van de frequentie van deze sprongen bevat veel parallellen met nucleatietheorie, maar sommige complicerende factoren, bijvoorbeeld de kromming

van het grensvlak, zijn niet aanwezig. We vinden overeenstemming tussen de theoretisch voorspelde sprongfrequenties en de simulatieresultaten.

In hoofdstuk 3 en 4 presenteren we resultaten van computersimulaties van nucleatie in het Isingmodel met een extern veld waardoor een van de twee fasen niet langer stabiel is. De gemeten nucleatietijden in simulaties die beginnen in de metastabiele fase worden vergeleken met de voorspellingen van klassieke nucleatietheorie. De simulaties en de theorie blijken goed overeen te stemmen als eindige-afmetingseffecten in rekening worden gebracht. Ook blijkt het nodig te zijn de snelheid waarmee clusters van verschillende groottes groeien en krimpen in detail te bekijken.

In hoofdstuk 5 wordt de analysemethode van het voorgaande hoofdstuk toegepast op een heel ander systeem: de fluctuaties van het aardmagnetisch veld over lange tijden (duizenden jaren). Dankzij deze methode kunnen we achterhalen dat de ruis die verantwoordelijk is voor de fluctuaties meer overeenkomt met additieve ruis dan met multiplicatieve ruis. Dit is in strijd met de tot dusver bekende theoretische voorspellingen.

# Curriculum Vitae

The author of this thesis was born on February 25 1977 in Amsterdam. From 1989 to 1995 he attended the Stedelijk Gymnasium Johan van Oldenbarnevelt in Amersfoort. From 1995 to 2001 he studied physics at the University of Utrecht, where he wrote his Master thesis under the supervision of prof. Tjon. The title was "Effective Field Theory of the Two Nucleon Interaction". From 2001 to 2005 he did his Ph.D. research under the supervision of Gerard Barkema and Henk van Beijeren.